Electrochemical Corrosion Testing of Neutron Absorber Materials

Tedd Lister
Ron Mizia
Arnold Erickson
Tammy Trowbridge

May 2007

INL
Idaho National Laboratory

Electrochemical Corrosion Testing of Neutron Absorber Materials

Tedd Lister
Ron Mizia
Arnold Erickson
Tammy Trowbridge

May 2007

Idaho National Laboratory
Idaho Falls, Idaho 83415

Electrochemical Corrosion Testing of Neutron Absorber Materials

INL/EXT-06-11772, Rev. 1

Approved by

_____
T.E. Lister

$6/25/07$
_____
Date

_____
R.E. Mizia

$6-25-07$
_____
Date

S. MBWR
_____
S.M. Birk

$6-25-07$
_____
Date

CONTENTS

FIGURES

vi

TABLES

ACRONYMS

ASME   American Society of Mechanical Engineers

ASTM   American Society for Testing and Materials

BSC   Bechtel SAIC, LLC

BSE   backscatter electron

CR   corrosion rate

DOE-EM   Department of Energy Office of Environmental Management

DOE-RW   Department of Energy Office of Civilian Radioactive Waste Management

HIP   hot isostatic pressing

INL   Idaho National Laboratory

LLNL   Lawrence Livermore National Laboratory

LOM   light optical microscopy

LPR   linear polarization resistance

LTCTF   Long Term Corrosion Test Facility

MCA   multiple crevice assembly

NSNFP   National Spent Nuclear Fuel Program

PD   potentiodynamic

PS   potentiostatic

QARD   Quality Assurance Requirements and Description

SCE   saturated calomel electrode

SCMW   simulated cement modified water

SD   standard deviation

SE   secondary electron

SEM   scanning electron microscopy

SNF   spent nuclear fuel

SNL   Sandia National Laboratory

TAD	transport, aging, and disposal
UNS	Unified Numbering System
XRD	x-ray diffraction
YMP	Yucca Mountain Project

Electrochemical Corrosion Testing of Neutron Absorber Materials

1.   INTRODUCTION

The Yucca Mountain Project (YMP) was directed by the Department of Energy Office of Civilian Radioactive Waste Management (DOE-RW) to develop a new repository waste package design based on the transport, aging, and disposal (TAD) canister system concept. The waste package is the disposal container that the TAD canister will be sealed inside prior to its disposal in the repository. A neutron poison material for fabrication of the internal spent nuclear fuel (SNF) baskets for these canisters is required. Borated stainless steel has been used for criticality control for the wet storage and transportation of SNF.[1,2,3] These stainless steel products are available as an ingot metallurgy plate product (Neutronit A978), which is basically a 316 stainless steel composition with a higher chromium level with a boron addition[a] and powder metallurgy product (Neutrosorb Plus)[b] that meets the requirements of American Society for Testing and Materials (ASTM) A887, Grade A.[1]

The YMP originally specified that the Neutronit A978 borated stainless steel be used for the commercial spent-fuel, internal-basket structure in the waste package.[4] During this time, a new Ni-Cr-Mo-Gd alloy[5] was developed by Idaho National Laboratory (INL), with its research partners Sandia National Laboratory (SNL) and Lehigh University. The Department of Energy Office of Environmental Management (DOE-EM) provided funding for the alloy development through the National Spent Nuclear Fuel Program (NSNFP). The NSNFP designated this neutron-absorbing alloy for fabrication of the SNF baskets in the DOE standardized canister. INL has designed the DOE Standardized Spent Nuclear Fuel Canister[6] for the handling, interim storage, transportation, and disposal of DOE-owned SNF in the repository. The DOE canisters will be placed in a waste package prior to their disposal in the repository.

The contractor for the Yucca Mountain Project, Bechtel SAIC, LLC (BSC), later selected the Ni-Cr-Mo-Gd alloy as a neutron absorber for commercial SNF baskets based upon poor corrosion performance of Neutronit A978 alloy in long-term corrosion tests in acidic waste-package environments. Since then, waste-package chemistry modeling at the YMP determined the environment to be more benign (lower temperature, less acidity) than previously estimated. In addition, TAD canister vendors expressed concern about the Ni-Cr-Mo-Gd alloy's fabricability and commercial availability and the lack of neutronics experience with the alloy. Consequently, BSC asked INL to conduct comparative testing (work performed to best laboratory practices though not in compliance with all quality assurance requirements and description [QARD][7] criteria) of Neutronit A978 (ingot metallurgy, hot rolled) with Neutrosorb Plus 304B4 Grade A (powder metallurgy, hot rolled) and the Ni-Cr-Mo-Gd alloy (ingot metallurgy, hot rolled) to examine the performance of these alloys in the more benign environment. Results were documented in the first version of this report and indicated significantly lower corrosion rates for the borated stainless alloys than those measured in the long-term test's more-aggressive conditions. These results were the basis of the DOE recommendation that Type 304B4, grade A borated stainless steel be selected as the neutron absorber material used for the internal basket structure in the TAD canister specification for commercial fuels.

In 2007, SNL asked INL to repeat the corrosion tests on the existing Type 304B4, Grade A specimens in strict compliance with the QARD criteria, such that results could be used in future quality-affecting analysis and modeling reports. The results of that work are found in INL/EXT-07-12633.[8] In addition,

---

[a]. Bohler Bleche GmbH, P.O. Box 28, Murzzuschlag, Austria.

[b]. Carpenter Technology Corp. P.O Box 14662, Reading, PA.

SNL asked INL to conduct some additional tests (work performed to best laboratory practices though not in compliance with all quality assurance requirements and description [QARD] criteria) to determine if the amount of boron in Types 304B5, Grade A and Type 304B6 Grade A would influence localized corrosion. Tests were also conducted to compare the Ni-Cr-Mo-Gd alloy with the well-characterized Alloy 22. An additional study was requested to determine where the boron went if localized corrosion occurred on these alloys. These additional tests are included in the revision to this report.

This report summarizes the results of crevice-corrosion tests for six alloys in solutions representative of ionic compositions inside the waste package should a breach occur. The alloys in these tests are Neutronit A978[a] (ingot metallurgy, hot rolled), Neutrosorb Plus 304B4 Grade A[b] (powder metallurgy, hot rolled), Neutrosorb Plus 304B5 Grade A[b] (powder metallurgy, hot rolled), Neutrosorb Plus 304B6 Grade A[b] (powder metallurgy, hot rolled), Ni-Cr-Mo-Gd alloy[2] (ingot metallurgy, hot rolled), and Alloy 22 (ingot metallurgy, hot rolled).

2.   MATERIAL DESCRIPTIONS

2.1   Borated Stainless Steel

2.1.1   Physical Metallurgy

The borated stainless steel alloys solidify as primary austenite with a terminal eutectic constituent, which has the form Fe_2B, Cr_2B, with the exact composition dependent on the initial boron level.[9] A light optical micrograph (LOM) of an ASTM A887, Grade A material is shown in Figure 1. The austenite matrix is a ductile phase, and the dispersed secondary phase is a comparatively brittle compound. The ingot-metallurgy product microstructure of Neutronit A 978 is shown in Figure 2. In general, the powder-metallurgy product will have smaller, more circular borides than the ingot-metallurgy product, which will improve mechanical properties (impact strength and tensile ductility).[10]

Cr_2B, Fe_2B →

25 µm
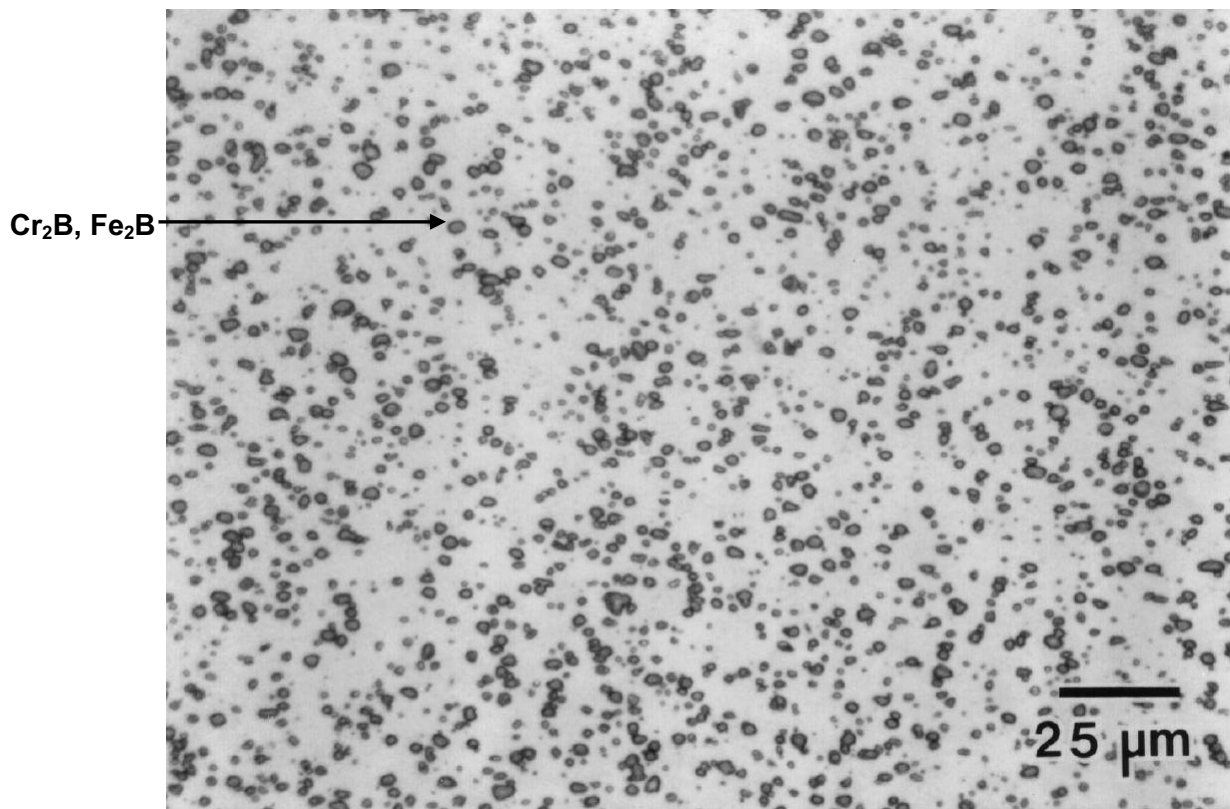
Figure 1. Light optical micrograph (LOM) image of 304B4A (Heat 182194), powder metallurgy, hot rolled.

Cr$_2$B, Fe$_2$B
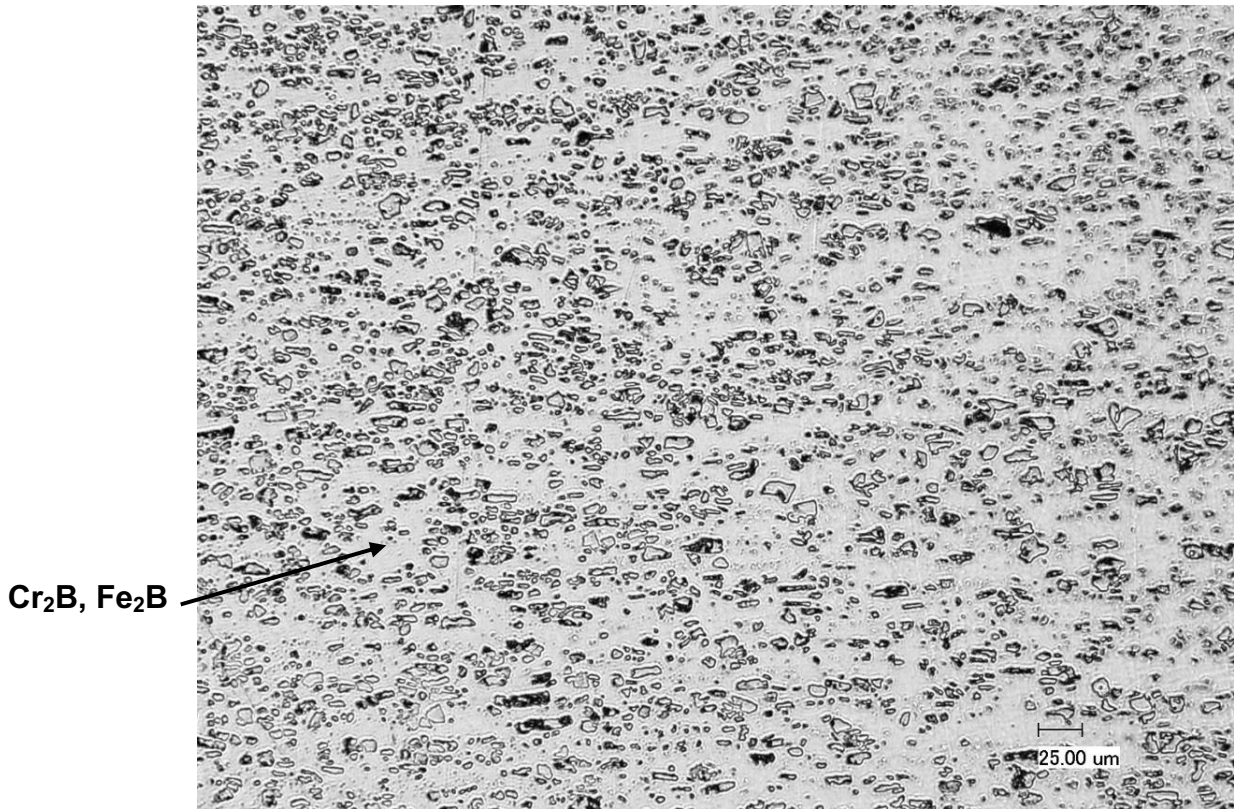
Figure 2. LOM image of Neutronit A 978 (Heat E084295).

2.1.2   ASTM and ASME Standards

Borated stainless steels are defined in ASTM A887 [1] where there are eight types (304B–304B7), which define boron concentrations from 0.2 to 2.25 wt%. There are two grades (A and B) defined where requirements are controlled by mechanical properties. These requirements essentially define the alloy processing where Grade A alloys are powder-metallurgy products and Grade B alloys are ingot-metallurgy products. There are 16 discrete alloys specified in ASTM A887. The Grade A materials used for this testing (heats 182194, 182195, 182196) were fabricated by CARTECH using the powder metallurgy process. This involves full density consolidation of inert-gas atomized powders by hot isostatic pressing (HIP). The HIP compacts were forged and hot rolled into a plate. The as-received plate has the HIP can material (Type 304 stainless steel) on the top and bottom surfaces, which was removed by machining during the coupon fabrication process to test the borated stainless steel matrix only. The Neutronit A978 alloy is an ingot-metallurgy product where a boron addition is made to a 316 stainless steel alloy chemistry. The chemical composition and mechanical properties of Neutronit A978 are not defined in ASTM A887.

The American Society of Mechanical Engineers (ASME) design allowables are defined in Code Case N-510-1. [11]

4

2.2   Ni-Cr-Mo-Gd Alloys

2.2.1   Physical Metallurgy

A typical microstructure for the Ni-Cr-Mo-Gd alloy is shown in Figure 3. The microstructure consists of a Ni-Cr-Mo austenitic matrix (darker structure), which has a composition similar to UNS N06455 (Alloy C-4), and a dispersed secondary phase (lighter structure), which has a hexagonal crystal structure and a phase composition of Ni_5Gd.
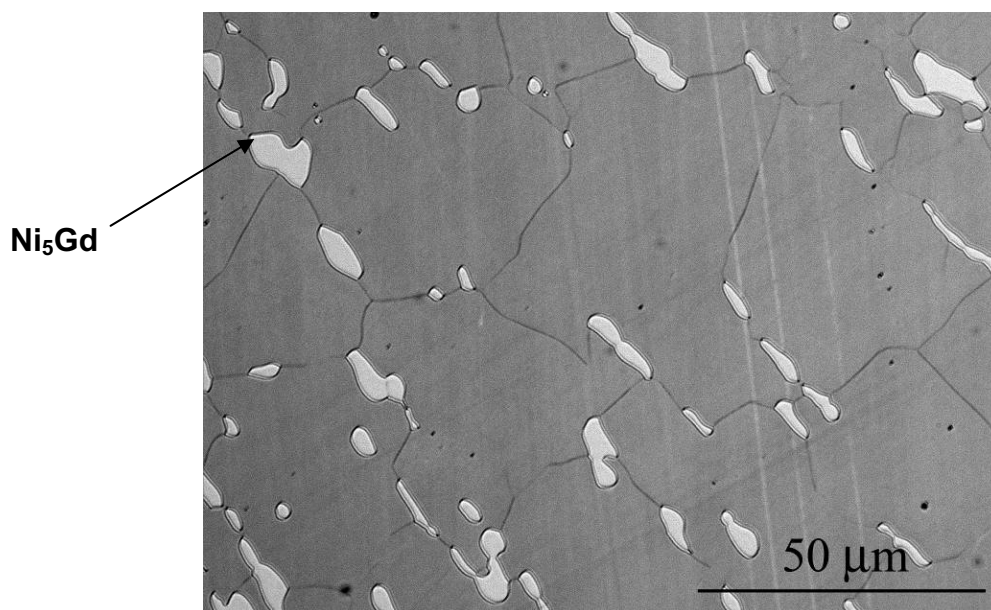
Figure 3. LOM image of Ni-Cr-Mo-Gd alloy microstructure.

This secondary phase is generally found at the austenite grain boundaries. The Ni_5Gd phase (referred to as a gadolinide in this report) also contains small amounts of dissolved chromium and molybdenum (on the order of 1 wt%). The size, shape, and distribution of the secondary phase evolves from its initial solidification morphology in the interdendritic regions of the as-cast ingot through hot rolling and heat treatment to the wrought structure illustrated in Figure 3. Gadolinium has extremely limited solubility in the nickel austenite matrix. As in the case of the borated stainless steels, the alloy can be described as containing a hard-dispersed secondary phase within a softer, ductile austenitic matrix.

2.2.2   ASTM and ASME Standards

The Ni-Cr-Mo-Gd alloy chemistry requirements are defined in ASTM B932-04.[5] The mechanical and physical property requirements and ASME design allowables are defined in ASME Code Case N-728.[12]

2.3   Experimental

2.3.1   Specimens for 60°C Testing

Table 1 shows the composition of the alloys used for testing. The A978 specimens were refinished from coupons previously used for the YMP corrosion studies (culled for the least amount of damage) by Lawrence Livermore National Laboratory (LLNL) (Heats E084295 and N156129).[13] These specimens

had been used for long-term immersion tests and were not designed for electrochemical testing. The size of the furnished specimens did not allow fabrication of the crevice specimens used for the other alloys.

Table 1. Alloy composition (wt%) for borated stainless steel and Ni-Cr-Mo-Gd.

	304B4 Grade A	304B5 Grade A	304B6 Grade A	ASTM B 932-04 (Ni-Cr-Mo-Gd)	Neutronit A978	Neutronit A978
Heat #	182194	182195	182196	D5-8235	N156129	E084295
Name	304B4	304B5	304B6	Ni-Cr-Mo-Gd	316B(SSN)[13]	316B(SSE)[13]
Cr	19.46	19.36	19.04	16.75	19.16	18.18
Ni	13.39	13.39	12.78	Bal	12.74	12.07
Mo	-	-	-	14.43	2.22	2.11
B	1.17	1.32	1.69	-	1.17	1.00
Gd	-	-	-	1.89	-	-
C	0.05	0.05	0.05	0.003	0.039	0.056
Mn	1.91	1.84	1.69	<0.01	0.097	1.70
Cu	-	-	-	-	0.10	0.35
Fe	Bal	Bal	Bal	<0.01	Bal	Bal

Specimens of Types 304B4A, 304B5A, 304B6A, and the Ni-Cr-Mo-Gd alloys were machined from plate stock. To ensure that only the borated stainless steel matrix was tested, the as-received plate (304B4A, 304B5A, 304B6A,) had the HIP can material (Type 304 stainless steel) removed from the top and bottom surfaces. The crevice specimen design is based on the LLNL specimen design and is described in a controlled INL document.[14] The 304B4A, 304B5A, 304B6A, and Ni-Cr-Mo-Gd specimens were 0.75 in. × 0.75 in × 0.375 in., with a 0.28-in. through-hole for the crevice assembly. The A978 specimens obtained from LLNL were approximately 1 in. × 1 in. × 0.125 in., with a 0.3-in. through-hole for the crevice assembly. The specimens were wet sanded with 240- and 600-grit SiC paper the day of testing.

The crevice formers used in the test were made of ceramic in a multiple crevice assembly (MCA) design. The surfaces were wet sanded with 600-grit SiC paper to smooth the as-received surfaces. The crevice formers were attached to the specimens with fasteners made of alloy C-276. Teflon tape was wrapped on the crevice bolt to electrically isolate it from the specimen. A torque of 50 in./Oz was applied to the crevice bolt for all tests. The Teflon tape used in earlier testing was not used to create a tight crevice in the MCA. Teflon MCA washers were used in some cases.

A special electrical contact was needed for the A978 specimens due to the lack of width for a conventional attachment. Platinum wire was spot-welded to the specimen surface, and an electrical lead wire was soldered to the platinum. The exposed wires were isolated using epoxy designed for submersion conditions. Problems with the epoxy occurred in some tests, as is discussed in Section 3.2.5 and Appendix A. A second set of tests were performed using a platinum wire spot-welded to the specimen extending outside the cell without any coating. This appeared to affect the results and is discussed in Appendix A.

2.3.2   Specimens for 90°C

Additional crevice corrosion tests were performed on three Ni-based alloys in a potentiostatic (PS) electrochemical test. The purpose of these tests was to compare the performance of the Ni-Cr-Mo-Gd alloy to a well-characterized material, Alloy 22. The two Ni-Cr-Mo-Gd alloys are designated as M340

and M327, the main difference between the alloys being the chromium level where the M327 matches the Alloy 22. The Alloy 22 specimen was machined for YMP studies by LLNL. Table 2 shows the composition of the alloys used in the tests.

Table 2. Alloy composition (wt%) for Ni-Cr-Mo-Gd and Alloy 22.

Element	M340	M327	Alloy 22
Cr	15.25	21.01	21.23
Mo	14.07	14.3	13.37
Gd	1.99	1.98	0
W	n/a	n/a	2.93
Fe	0	0	3.65
Co	0	0	1.7
Ni	Bal	Bal	Bal

The outer surfaces of the specimens were sequentially ground with 240- and 600-grit SiC paper. The surface area was calculated from measurements of the specimen dimensions using calibrated calipers. The specimens were degreased (acetone and ethanol) and weighed prior to testing. MCA ceramic washers (12 tooth, OD 1.6 cm, ID 0.65 cm) were used with Teflon tape (1-1/2-in.-wide military grade) placed between the specimen surface and the crevice washer. The crevice bolt was alloy C-276 and was tightened to 70 in./lb. Teflon compression washers were used to connect the assembly to the specimen holder. The surface area was approximately 16 cm^2.

2.3.3   Solutions for 60°C Testing

The compositions of the three solutions used in these tests are shown in Table 3. These compositions were supplied by the YMP technical staff.[15] These solutions are based on expected compositions (major ions) for in-package chemistry. Each solution was mixed in a large batch, such that all solutions of that type were the same. Chemicals were American Chemical Society grade and used exclusively for this work. The nitrate-to-chloride and nitrate-to-halide ratios are calculated for comparison purposes. For these tests, only solutions B1 and B3 were used.

Table 3. Solution compositions for 60°C testing.

Test Solution	[Cl$^-$] (m)	[F$^-$] (m)	[NO$_3^-$] (m)	pH	NO$_3$/Cl	NO$_3$/(Cl+F)
B1	0.004	0	0.005	7	1.25	1.25
B2	0.004	0.001	0.005	5.5	1.25	1.00
B3	0.004	0.001	0.0025	5.5	0.63	0.50

2.3.4   Solutions for 90°C Testing

The high-halide, low-pH solution used in the test was modeled as a worst-case solution from the modeled range of composition for in-package chemistry of breached waste canisters,[16] which contained carbon steel structural tubing. The test solution chemistry is shown in Table 4.

Table 4. High-halide, test-solution composition.

Test Solution	[Cl⁻] (m)	[F⁻] (m)	[NO₃⁻] (m)	pH	NO₃/Cl	NO₃/(Cl+F)
High halide, low pH	6×10^{-3}	1×10^{-2}	7.3×10^{-4}	4.5	0.122	0.046

2.3.5 Testing Procedures for 60°C Tests

The testing procedures are contained within the INL document, PLN-1885.[17] The cell was similar to that described in ASTM G5, Figure 3.[18] All tests were performed at 60°C, maintained by a thermocouple-based temperature controller. The heating was supplied by a mantle under the cell. The temperature of the cell was confirmed using a calibrated thermometer before the initiation of each test. The cell was fitted with a condenser to prevent solution loss during the test. Chilled water (5°C) was passed through the condenser. The reference electrode was contained in a water-chilled Luggin capillary. A single graphite rod was employed as the counter electrode.

2.3.6 Testing Procedures for 90°C Tests

The testing procedures are contained within the INL document PLN-1885.[17] The cell was similar to that described in ASTM G5, Figure 3.[18] All tests were performed at 90°C, which was maintained by a thermocouple-based temperature controller. The heating was supplied by a mantle under the cell. The temperature of the cell was confirmed using a calibrated thermometer before the initiation of each test. The cell was fitted with a condenser to prevent solution loss during the test. Chilled water (5°C) was passed through the condenser. The reference electrode was contained in a water-chilled Luggin capillary. A single graphite rod was employed as the counter electrode. The PS test was performed at 0.20 V versus saturated calomel electrode (SCE) in the high-halide solution at 90°C. The test time was 7 days.

2.4 Examination of Borated Stainless Steel Corrosion Products

As directed by the Technical Work Plan,[19] an examination of the borated stainless steel corrosion products was performed to determine the presence and condition of chromium and iron boride particles. The objective was to determine if chromium/iron boride particles survive corrosion and remain behind in the corrosion products, survive corrosion and are swept away, or dissolve and put the boron into solution. These results can have potential impacts to long-term criticality control.[19]

Because there was not sufficient corrosion product from the testing of the Grade A materials, previously provided specimens from the longer-term corrosion tests performed at LLNL were used.[13] These samples were analyzed using scanning electron microscopy with energy-dispersive x-ray spectroscopy to determine the disposition of chromium/boride particles in the corrosion products. An additional corrosion product from one sample was analyzed with x-ray diffraction (XRD).

2.4.1 Microscopy

The INL scanning electron microscopy (SEM) instrument is a Phillips XL30 ESEM with a LaB₆ filament. The Energy Dispersive X-Ray Spectrometer detector is an EDAX Genesis with a Super Ultra Thin Window. The SEM conditions included a 20 kV accelerating potential with an interaction volume for this material of approximately 1.2 µm. The lighter elements, including boron, were detected using the same system with conditions of 10 kV accelerating potential. The analysis software is EDAX Genesis with ZAF corrections. A general standard set (aluminum and copper) were used to calibrate peak height and position. The samples were lightly coated with platinum. Count times for mapping were taken, such

that a sufficient point map could be extracted from the corresponding SEM image. These times ranged from 1500–5000 Ms per point, with a consistent 128 frames taken for each data set.

3.   RESULTS AND DISCUSSION

3.1   Potentiodynamic Tests

Potentiodynamic (PD) tests at 60°C were performed in solution B1 as a preliminary investigation of the corrosion properties of these materials. These tests were performed to be consistent with ASTM G5 testing protocols. A cyclic potential profile was used to investigate the repassivation characteristics of the materials on the return sweep. Heat E084295 was used for the A978 specimen. The PD test was initiated after performing a 50-min corrosion potential (E_{corr}) measurement with N_2 purge. The PD scan was initiated -0.2 V negative of the measured E_{corr} and reversed at +0.8 V versus a SCE. The scan rate was 0.166 mV/sec. Note that the electrical contact for the A978 specimen in this short-period test did not appear to be compromised, as was the case for later PS tests; therefore, the data is included in Figure 4.

PD curves of the three specimens are shown in Figure 4, with the E_{corr} breakdown potentials (E_{bd}) and repassivation (E_{rp}) values provided. The A978 specimen had a breakdown value (using a 10 μA/cm^2 criteria; see the dashed blue line on the plot in Figure 4) approximately 0.2 V negative of the 304B4 specimen, indicating a greater tendency to pitting. The E_{bd} value for Ni-Cr-Mo-Gd is very close to the E_{corr} value indicating a very reactive surface due to the initial gadolinide dissolution. The E_{rp} value (using the crossover criteria) for A978 is about 0.14 V more negative than 304B4, indicating a reduced tendency to repassivate, as compared to the 304B4 specimen under these conditions. The total current passed during breakdown is also much greater for the A978. The Ni-Cr-Mo-Gd has a much higher current in the forward sweep but a reduction in current during the reverse sweep. Thus, no E_{rp} value applies. The measurements are consistent with the observations of the specimen as discussed in the next paragraph.
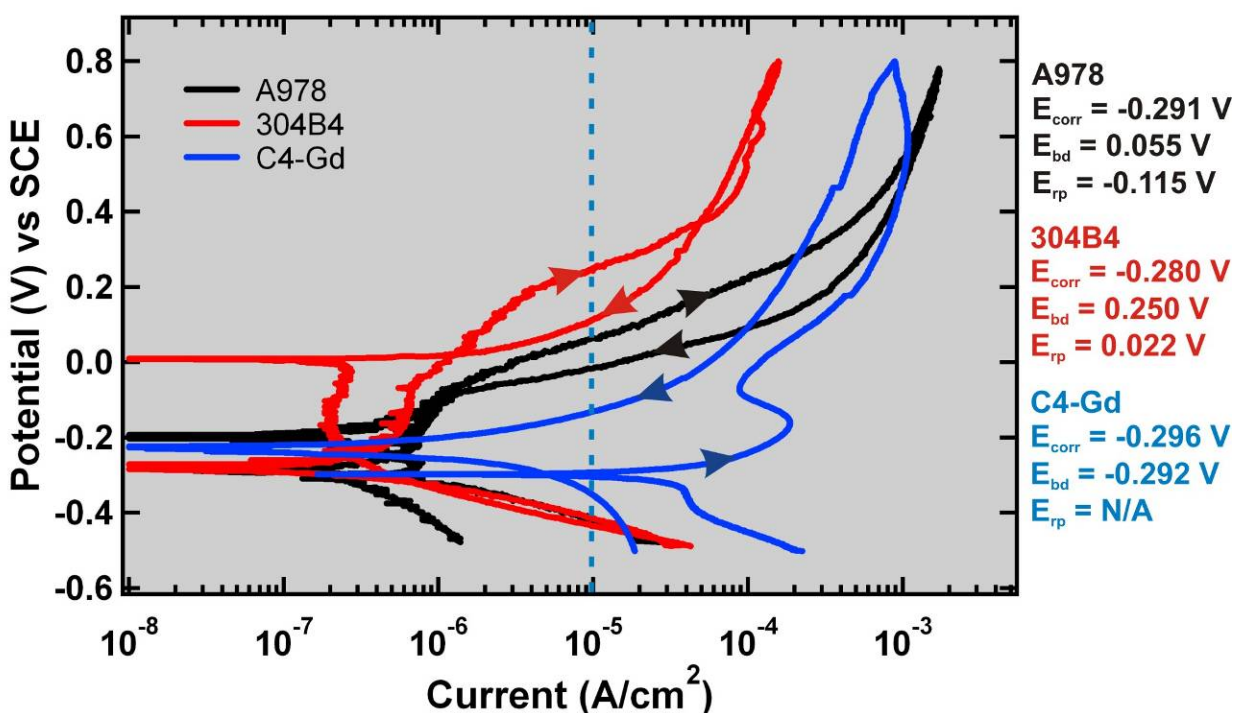
Figure 4. Potentiodynamic (PD) curves for the three alloys in solution B1 at 60°C

Photographs of the specimens after the PD testing are shown in Figure 5. The specimens show attack occurring primarily at the base metal/MCA teeth interface. The A978 specimen showed much greater crevice attack with 20 of the 24 teeth showing crevice attack. The 304B4 showed attack in 9 of the 24 teeth, with the total damage area/damaged area under the MCA teeth being lower. The Ni-Cr-Mo-Gd alloy did not show any extensive etching or pitting under the crevice teeth. There are stains outside the crevice regions. These stains were likely caused by corrosion products leeching from within the crevice areas (lower pH) and precipitating into high-pH regions.
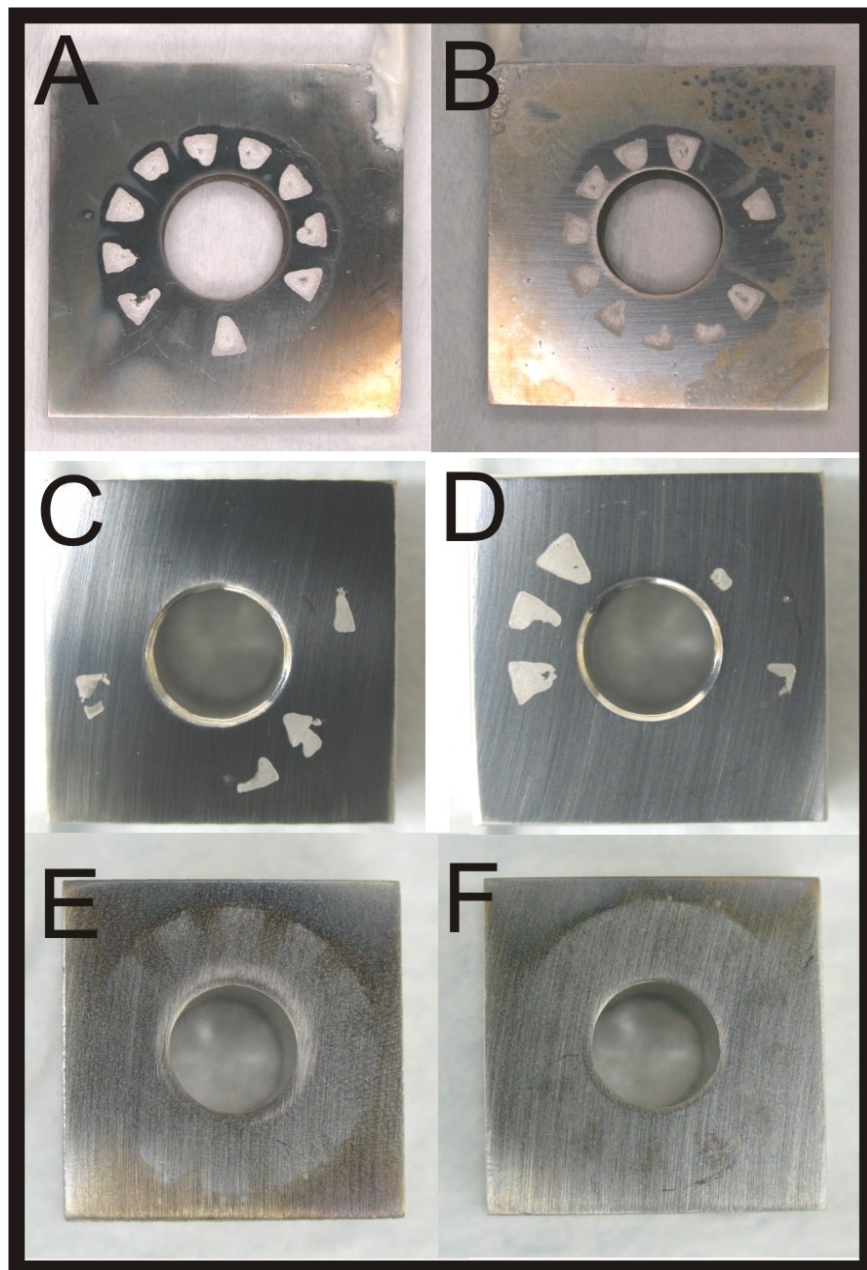
Figure 5. Macro photographs of A978 (A and B), 304B4 (C and D), and Ni-Cr-Mo-Gd (E and F) after PD testing.

LOM images of the specimens are shown in Figure 6. It is apparent that significant crevice corrosion occurred under the MCA teeth of the borated stainless steel specimens. The damage was more pronounced on the A978 specimen. There was also pitting outside the crevice area (see Figure 6, B and C) on the A978 specimen, while none was observed on the 304B4 specimen. The Ni-Cr-Mo-Gd alloy shows the removal of the gadolinide particles through dissolution. This observation agrees with the large anodic current observed in the forward sweep.
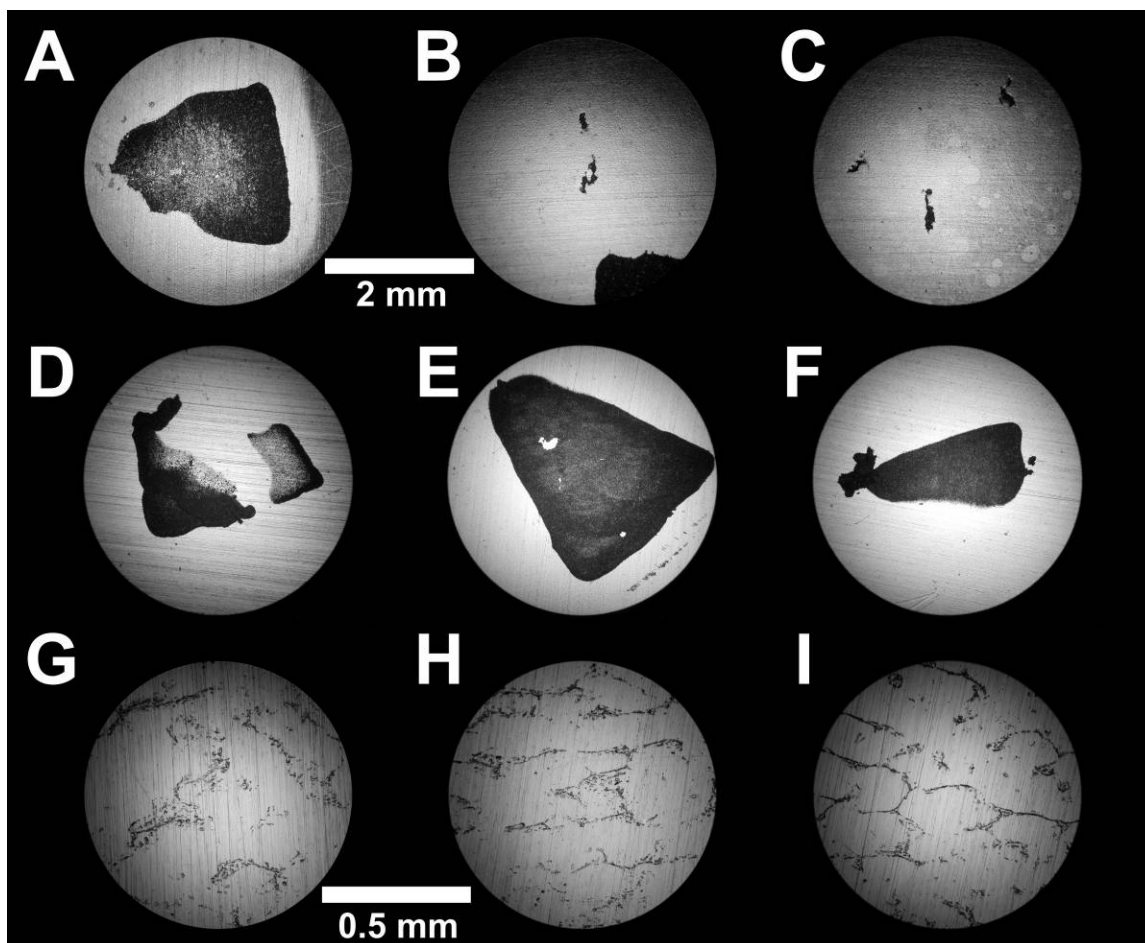
Figure 6. LOM images taken at 50× magnification factor for A978 (A–C) and 304B4 (D–F) and at 200× magnification factor of Ni-Cr-Mo-Gd (G–I) after PD testing.

As an additional part of the Ni-Cr-Mo-Gd corrosion testing, linear polarization resistance (LPR) sweeps were performed before and after the PD sweep. The corrosion rate before the sweep was 405 μm/year and dropped to 8.10 μm/year after the test. This decrease was due to removal of surface gadolinides. More details of the LPR sweep methods are provided in Section 3.2.

The superior performance of the 304B4 specimen over the A978 appears to be a metallurgical phenomenon. The A978 material is an ingot-metallurgy product and, thus, will have larger, more elongated secondary-phase (Cr_2B) particles, while the Neutrosorb Grade A product will have a more uniformly distributed, rounded secondary phase.[20] The Ni-Cr-Mo-Gd alloy shows a superior resistance to base material attack as evidenced by the lack of substantial crevice attack. The higher resistance to

crevice corrosion is related to the known localized, corrosion-resistance properties of the Ni-Cr-Mo-based composition of the Ni-Cr-Mo-Gd alloy.

3.1.1 Additional PD Testing Results

Figure 7 shows cyclic PD polarization scans for the four borated stainless steel specimens in B1 solution (see Tables 1 and 3). The solution was purged with N_2 during the entire test period. A 50-min E_{corr} measurement was performed before initiating the test sequence. The dotted line in Figure 7 indicates the breakdown threshold using a 10 $\mu A/cm^2$ criterion. Table 5 contains parameters obtained from the corrosion potential (E_{corr}) and PD curves. Note that the 304B5 has the most positive breakdown potential (E_{bd}), and the repassivation potential (E_{rp}) value is very similar to 304B4 (best performing). This observation is consistent with the low number of negative spikes in the aerated E_{corr} measurements for 304B5. The A978 specimen has the most negative values for E_{bd} and E_{rp} (worst performing). The 304B6 has a similar E_{bd} to 304B4 but has a much more negative E_{rp} that is similar to the A978. Because the 304B6 has significantly more B content than A978, the similar E_{rp} value indicates a microstructural effect. Thus, these tests show that the amount of boron and the alloy grade (microstructure) influence the localized-corrosion characteristics. In all cases, significant pitting was observed under the crevice formers. In some cases, pitting was observed on boldly exposed surfaces as well.
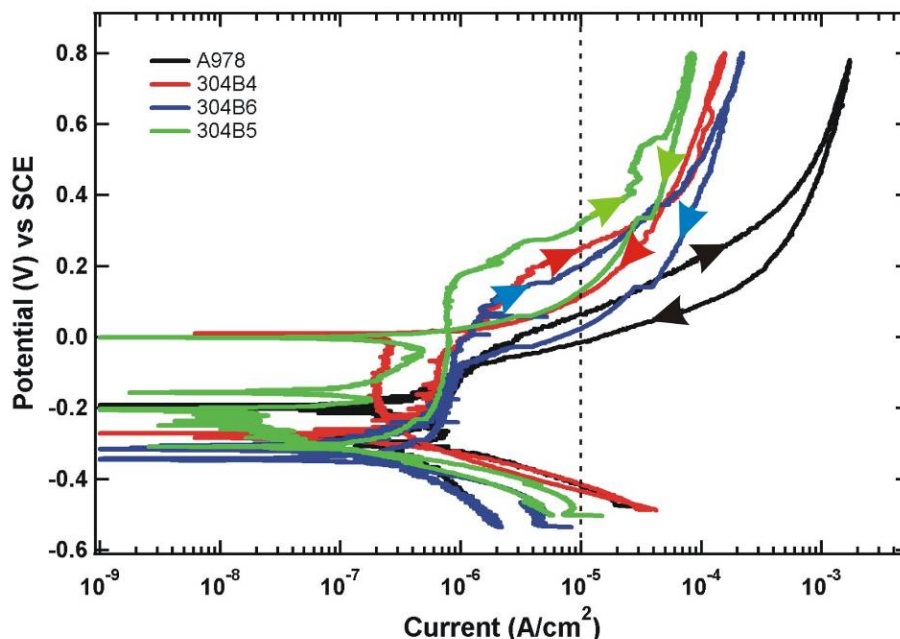
Figure 7. PD curves for borated SS alloys in solution B1 at 60ºC.

Table 5. Parameters obtained from PD curves in solution B1.

	304B4	304B5	304B6	A978
E_{corr}	-0.28	-0.3034	-0.3347	-0.291
E_{bd}	0.25	0.321	0.207	0.055
E_{rp}	0.022	0.018	-0.0943	-0.115

13

Additional PD tests were performed for the three Neutrosorb Plus alloys in solution B3 using Teflon MCA crevice formers. The curves from these tests are shown in Figure 8, with the data tabulated in Table 6. The E_{corr} values follow the trend of decreasing with increasing boron level. The E_{bd} potentials do not follow the trend of boron content because 304B5 has a higher E_{bd} value than 304B4. The E_{rp} values decrease with increasing boron level, as expected. A comparison of the alloys in the two solution types shows only a slight depression of the E_{corr} and E_{rp} values in B3, which is a significantly lower $NO_3/(Cl+F)$ value. The E_{bd} values are actually higher in the B1 solution, which is counter to the effect of halides. It is thought that at these low ionic contents the concentration of halides, which contribute to enhanced corrosion, must be less of an influence in localized corrosion processes. More testing would be required to make any significant statements about these results because they are based on single observations.
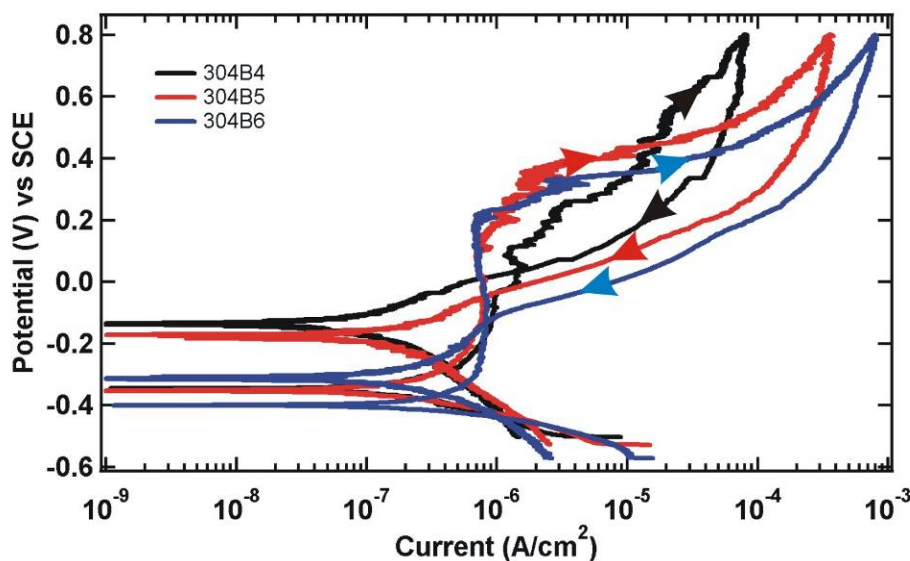
Figure 8. PD curves in solution B3 using Teflon multiple crevice assembly (MCA) crevice formers.

Table 6. Parameters obtained from PD curves in B3 solution.

	304B4	304B5	304B6
E_{corr}	-0.3031	-0.3283	-0.3728
E_{bd}	0.351	0.429	0.353
E_{rp}	0.032	-0.052	-0.137

3.2   PS Tests

3.2.1   PS Test Introduction

PS tests were used to determine the corrosion performance of the alloys over longer periods. In the case where no localized corrosion occurs, the current from the PS tests is directly proportional to the general corrosion rate. In the event that localized corrosion occurs during the PS test, the situation is not as straightforward. As localized corrosion by definition is not a uniform mechanism, the rate will not have the same meaning, but it is still proportional to the amount of material being removed. The rate is reported as a general corrosion rate in either case. The basis for calculation of the corrosion rate from the corrosion current (i_{corr}) can be found in ASTM G102[21] and is derived from Faraday's Law. As stated previously, the

corrosion rate assumes a uniform loss of material, which does not occur with localized processes, such as pitting, crevice corrosion, or dissolution of a secondary phase (i.e., the gadolinide phase in the Ni-Cr-Mo-Gd alloy).

The electrochemical potential chosen for the PS tests is based on what is expected in the environment. This was determined by measuring the E_{corr} for 24 hours while it was being saturating with air. This mimics the effect of maximum exposure of air, where oxygen acts as an oxidizer to shift the potentials of the materials in a positive direction. While general corrosion does not have a strong potential dependence, localized-corrosion initiation/propagation tends to increase with potential. The actual potential used for the tests was based on an early test for a 304B4 specimen where the E_{corr} value appeared to equilibrate between 0 and 0.1 V. Thus, while most of the tests were performed at 0.1 V, 0.2 V was also tested because higher aerated E_{corr} values for 304B4 were observed in other tests.

The PS curves obtained from these measurements also provide qualitative information. Ideally, general corrosion is a smooth current flow that decreases exponentially during the test. This has been observed in long-term corrosion testing of passive materials proposed for use by the YMP.[22] Localized corrosion can be ascertained if there are increases in current during the test. Metastable pitting events (the origins of pitting or crevice corrosion) are characterized by short-lived positive spikes in the current trace. Longer-lived events, beyond several seconds, are the result of sustained localized corrosion. The total charge is the integration of the current over the entire PS test. This provides a value for the total amount of material removed assuming the current is due to corrosion processes.

In addition, three LPR measurements were made just prior to the PS tests. These tests were performed after N_2 degassing for 24 hours to allow equilibration. The test involves scanning the potential at a slow scan rate (0.166 mV/sec), from -30 mV to +30 mV versus the measured E_{corr}. ASTM G59[23] describes the use of this technique in determining i_{corr} at open circuit potential (E_{corr}) using the Butler-Volmer relationship.[24] The slope of the curve is the polarization resistance (R_p) and has units of Ω-cm^2. The value of i_{corr} can be calculated if the Stern-Geary coefficient (B) is known. The three values were evaluated using the software package provided with the instrumentation. The linear portion of each curve was fit to determine the polarization resistance (slope of I-V curve). This was multiplied by the exposed surface area of the specimen. The value of (B) was estimated using Tafel slopes of 0.12 V/dec, yielding B = 0.0261 V. The i_{corr} was calculated using ASTM G59 Equation 2. The corrosion rate was calculated from i_{corr} as described previously for PS tests. A more advanced treatment uses a fitting procedure to determine the parameters in the event Tafel slopes are not known.[25] The corrosion rate is then calculated using the i_{corr} values, as described for the PS tests. Use of this method was not considered after very low cathodic Tafel slopes (below 5 mV/dec in most cases) were obtained. This is thought to be an issue with the software method of performing the sweep, where the step is immediately followed by the sweep. The fast drop in current and, consequentially, the low-calculated Tafel slope is due to capacitive discharge of the interface. Future studies will use a delay before the sweep is initiated.

The data for PS tests are contained in Table 7. Data from the A978 specimens are included in Appendix A. This should be referred to for the data sections that follow. In some cases, tests were interrupted by power failure (Tests 080806-1 and 080806-2) or problems with the reference electrode (Tests 080906-1 and 082106). The available data for these particular tests was placed in Table 7.

Table 7. Data obtained from electrochemical tests for borated stainless steel and Ni-Cr-Mo-Gd alloy.

Test ID	Alloy	Solution	Final E_{corr} Ox (V)	Final E_{corr} N_2 (V)	Potential (V)	Total Charge (C/cm^2)	Peak Current (A/cm^2)	i_{corr} (A/cm^2)	CR^a ($\mu m/yr$)
072406	304B4	B1	0.0331	-0.3011	0.1	4.44E-03	4.76E-06	3.42E-09	0.0325
072506	304B4	B3	0.0281	-0.3972	0.1	5.68E-03	6.69E-06	2.84E-09	0.0270
072606	304B4	B1	0.1781	0.04428	0.1	2.40E-03	2.03E-07	2.54E-09	0.0242
080806-1	304B4	B1	0.0697	-0.2493	0.1	N/A	N/A	N/A	N/A
080806-2	304B4	B1	0.1308	-0.1203	0.2	N/A	N/A	N/A	N/A
080906-1	304B4	B3	0.008	-0.29	0.1	3.65E-2	1.12E-04	1.24E-8	0.118
081406	Ni-Cr-Mo-Gd	B1	-0.3186	-0.3264	0.1	4.01	2.26E-04	1.63E-06	16.3
081706	Ni-Cr-Mo-Gd	B3	-0.259	-0.277	0.1	1.85	8.08E-5	1.01E-6	7.02
082106	Ni-Cr-Mo-Gd	B1	-0.3165	-0.3193	0.2	1.62	3.87E-4	9.36E-6	93.8
082406	Ni-Cr-Mo-Gd	B3	-0.2869	-0.3005	0.2	2.19	1.32E-4	3.49E-7	3.50

Notes: (numbers in red are incomplete data)

Tests 080806-1 and 080806-2 were interrupted by power outages, and potentiostatic (PS) data was lost

Test 080906-1 was interrupted by reference electrode problem after 2.07 days

Test 082106 was interrupted after 12 hours due to a bubble in the Luggin capillary

a. CR: corrosion rate

3.2.2 E_{corr} Measurements

The E_{corr} values measured under aeration demonstrated vastly different results for the borated stainless steels and the Ni-Cr-Mo-Gd alloy. The E_{corr} values were observed to shift positive of -0.1 V for the 304B4 alloy and as far positive as 0.178 V (Test 072606). Most tests showed E_{corr} values for 304B4 under aerated conditions between 0 and 0.2 V. These values should not be considered equilibrated because the potentials were trending positive at the end of the test. The values decreased to between -0.4 V and -0.25 V after the N_2 gas purge. The E_{corr} for the Ni-Cr-Mo-Gd was unaffected by the aeration, with observed values near -0.3 V. Examples of E_{corr} versus time are shown for conditions of aeration (see Figure 9) and N_2 gas purge (see Figure 10). The E_{corr} for the 304B4 alloy shows numerous negative excursions while being aerated. These are due to metastable (short-lived) pitting events. The E_{corr} for the Ni-Cr-Mo-Gd alloy does not show this type of activity, likely due to the corrosion potential being pinned to more negative potentials, which is due to the dissolution of the gadolinide phase.

Using the measured E_{corr} values observed for the 304B4 alloy, the potential for the PS tests was chosen to be 0.1 V. One test for 304B4, Test 072606, had a final E_{corr} value above 0.1 V. As will be discussed in Section 3.2.5, PS Measurements, a more positive value of 0.2 V was investigated as well. While the Ni-Cr-Mo-Gd showed much more negative values for E_{corr}, it is anticipated that the eventual removal of the surface intersecting gadolinide phase would result in E_{corr} values more like that of the 304B4.

Four tests were performed for the A978 alloy but are not shown. These tests had issues with specimen contacts, which are discussed in Section 3.2.5.
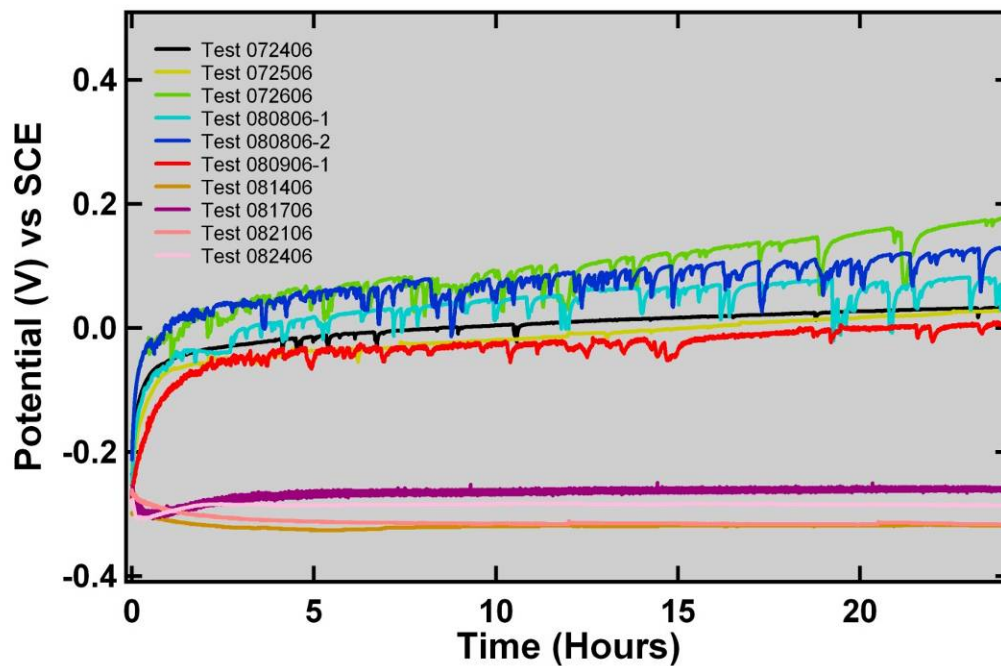

Figure 9. E_{corr} versus time for aerated cell. Tests 072406, 072506, 072606 080806-1, 080806-2, and 080906-1 are 304B4 specimens and test 081406, 081706, 082106, and 082406 are Ni-Cr-Mo-Gd specimens.

Figure 10. E_{corr} versus time for N_2 purged cell. Test 072406, 072506, 072606, 080806-1, 080806-2, and 080906-1 are 304B4 specimens, and tests 081406, 081706, 082106, and 082406 are Ni-Cr-Mo-Gd specimens.
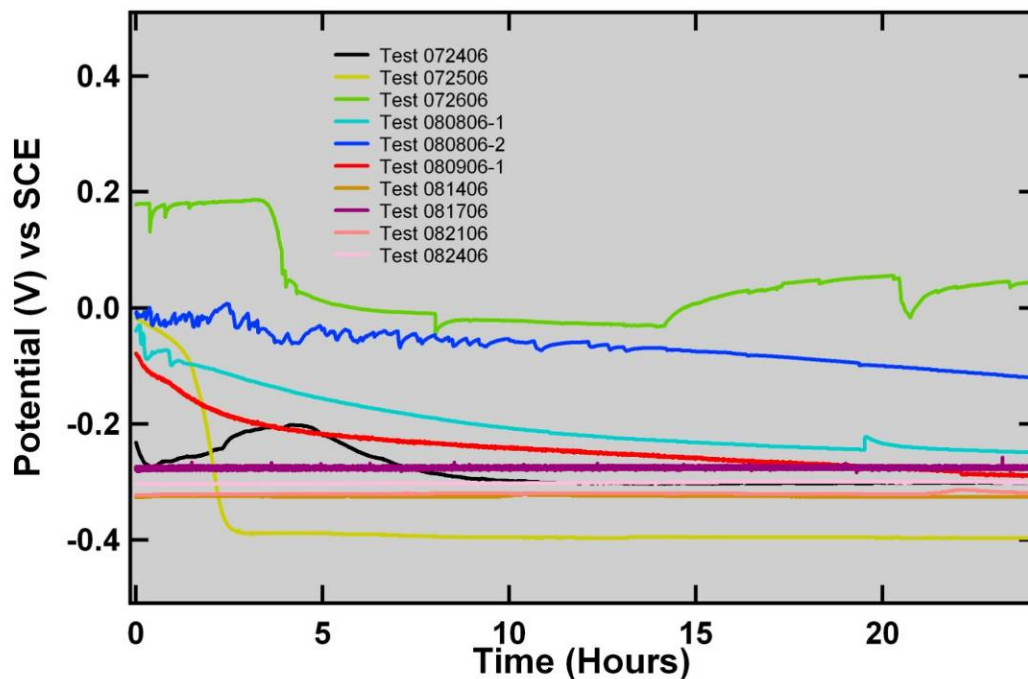
3.2.3   Additional Testing of Long-Term E_{corr} Tests

To determine the long-term E_{corr} value under aeration for 304B4 and 304B5 specimens, the E_{corr} was measured continuously for four consecutive 1-week periods at 60°C. Short gaps exist (up to several hours) where data was not collected. However, the data is plotted without these time gaps. Also note that the main specimen glassware joint showed condensation and precipitate from evaporative loss through that joint. Nanopure water was added to replace the water loss on a weekly basis. The precipitate was analyzed by XRD and was primarily NaCl and NaNO$_3$. Thus, the ionic composition was diluted over the testing period.

Figure 11 shows a plot of the data for specimens 304B5 and 304B6. The potential of both specimens rose in the initial hours to over 0 V, with 304B6 attaining the more positive value. The 304B6 specimen also had a significant number of negative spikes due to localized corrosion. After 2 weeks, some of the negative spikes are up to 0.3 V in magnitude and last for many hours. The 304B5 specimen showed few negative excursions comparatively. After 1 week, two LPR scans were performed on the 304B6 specimen while under aeration. The corrosion rate was 80 ± 3 nm/yr, indicating very low general corrosion rate in the passive region compared to those measured under N_2 purge in the PS tests, where the E_{corr} values were much more negative. The lower corrosion rate is due to the specimen residing in the passive region when aerated. After the tests, the specimen was examined with LOM, as shown in Figure 12. The most significant damage was observed at the Teflon compression gasket, where pitting around the circumference of the gasket was observed. Other less extensive pitting damage was observed under the MCA crevice formers. No significant damage to the 304B5 specimen with a ceramic MCA was observed.

18
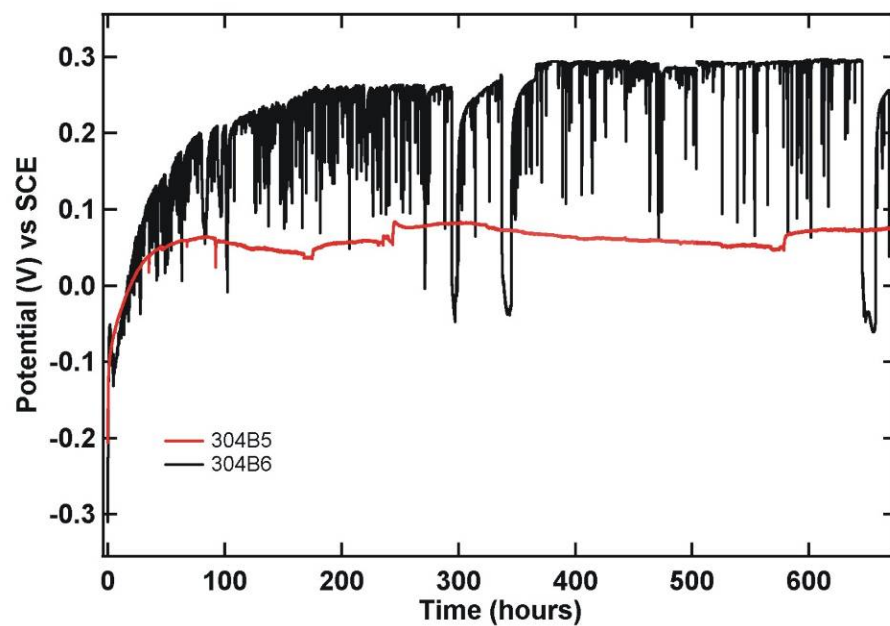
Figure 11. E_{corr} versus time for 304B5 and 304B6 specimens in solution B3 at 60ºC.
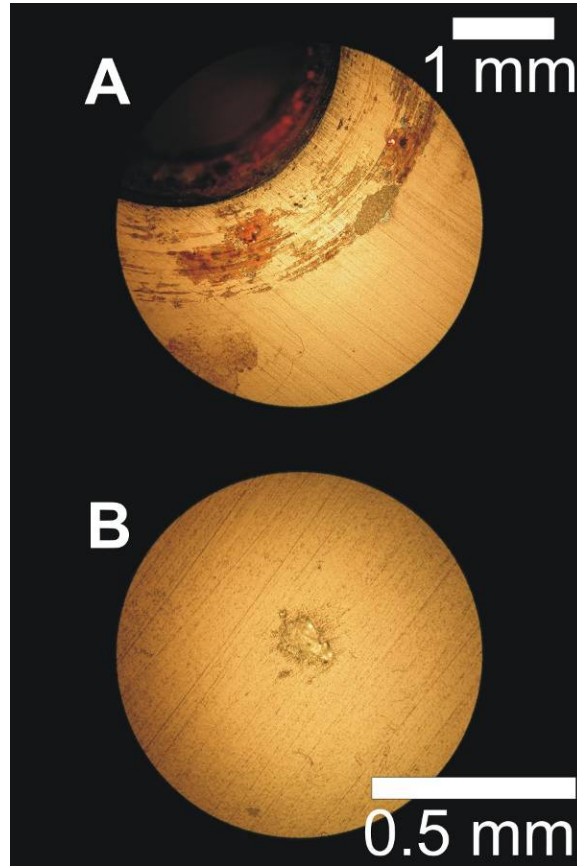
Figure 12. LOM of 304B6 specimen after 4 weeks at E_{corr}. Image (A) was taken from a compression gasket (50×) and image (B) was taken from an area under the MCA crevice former (200×).

An additional test using a 304B5 specimen was performed with a Teflon MCA and showed more negative excursions and a final potential that exceeded 0.2 V.This specimen did show limited crevice corrosion damage under the washer.

3.2.4   LPR Measurements

The corrosion rates calculated for LPR curves show that the 304B4 has lower corrosion rates than the Ni-Cr-Mo-Gd alloy. It is believed that the indicated corrosion rates for the Ni-Cr-Mo-Gd alloy are actually measuring the dissolution of the gadolinide secondary phase and are not indicative of the general corrosion rate of the base material. Table 8 shows the corrosion rates calculated from the LPR data. These results show the same trends observed in the PS tests described in Section 3.2.6.

Table 8. Corrosion rates from linear polarization resistance (LPR) measurements.

Test ID	Specimen Type	Avg. CR (μm/yr)	SD
72406	304B4	0.221	0.070
72506	304B4	0.276	0.057
72606	304B4	0.067	0.005
080806-1	304B4	0.197	0.072
080806-2	304B4	0.115	0.011
080906-1	304B4	0.647	0.049
81406	Ni-Cr-Mo-Gd	24.1	3.1
81706	Ni-Cr-Mo-Gd	5.19	0.067
82106	Ni-Cr-Mo-Gd	21.1	1.8
82406	Ni-Cr-Mo-Gd	1.85	0.960

3.2.5 PS Measurements

The PS measurements were performed primarily at 0.1 V, with 0.2 V used to determine the effect of higher potential in some tests. These values were derived from the E_{corr} measurements under aeration as described in Section 3.2.4. Figure 13 shows a plot of curves for the 304B4 and Ni-Cr-Mo-Gd alloys. In the case of 304B4, the current dropped to very low values at both potentials. The current translated into corrosion rates of less than 100 nm/year, which indicate very passive behavior. Spikes up to several hundred nA/cm^2 were observed during the tests, indicating metastable pitting activity, but no long-lived current excursions were observed. The total charge values were also very low, which is another indication that very little corrosion had occurred. Test 080806-2 was run at a higher potential of 0.2 V with similar behavior; however, a power outage resulted in the test ending early, and the data was lost. The data for the Ni-Cr-Mo-Gd alloy indicated lower general corrosion performance. This is likely due to the slow dissolution of the gadolinide phase. Steady decreases in current were observed for all Ni-Cr-Mo-Gd alloy tests. Longer test times or secondary-phase removal prior to testing should be considered to evaluate the true performance of the Ni-Cr-Mo-Gd alloy.

The four tests that were run with the A978 alloy are not shown in Figure 13 due to issues with these tests stemming from the design of the electrical contact. The first two tests used the epoxy-coated contacts, which delaminated after several days of exposure. After delamination, the contact corroded and contributed to the measured current. The second two tests used an exposed platinum wire contact that appeared to affect the potential and current during the tests. Small negative currents were observed for these final tests that are likely indicative of reactions on platinum. One crevice corrosion site was observed for Test 080206.
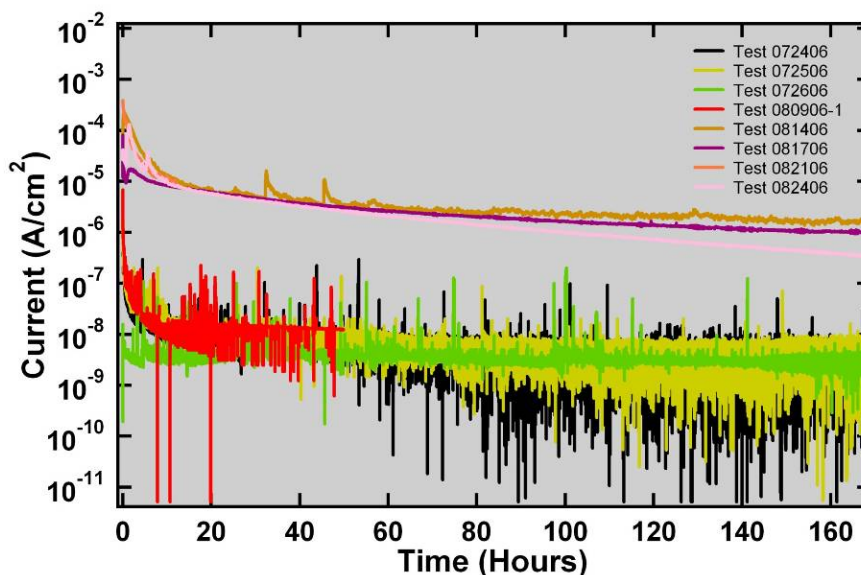
Figure 13. Current versus time plots for potentiostatic (PS) tests. Test 072406, 072506, 072606, and 080906-1 are for 304B4 specimens, and Tests 081406, 081706, 082106, and 082406 are Ni-Cr-Mo-Gd specimens. Note that Tests 080906-1 and 082106 are not complete 7-day data sets.

3.2.6   Additional PS Testing of Borated Stainless Steel at 60°C

Additional PS tests were performed on specimens of 304B4, 304B5, and 304B6 using the protocol employed in FY-06 testing of neutron absorbing alloys: (1) measurement of E_{corr} under aeration for 24 hours, (2) measurement of E_{corr} under N_2 purge for 24 hours, (3) followed by three LPR scans, and (4) 7-day PS hold at 0.1 or 0.2 V versus SCE.[26] The testing was performed in solution B3.

Figure 14 shows the E_{corr} data for 304B4, 304B5, and 304B6 under aeration and N_2 purge. The E_{corr} increases with time under aeration into the passive region. The negative excursions are localized corrosion initiations. The 304B6 specimen showed much more activity than the lower boron-containing alloys. Purging with N_2 resulted in the potential dropping to below -0.3 V versus SCE.
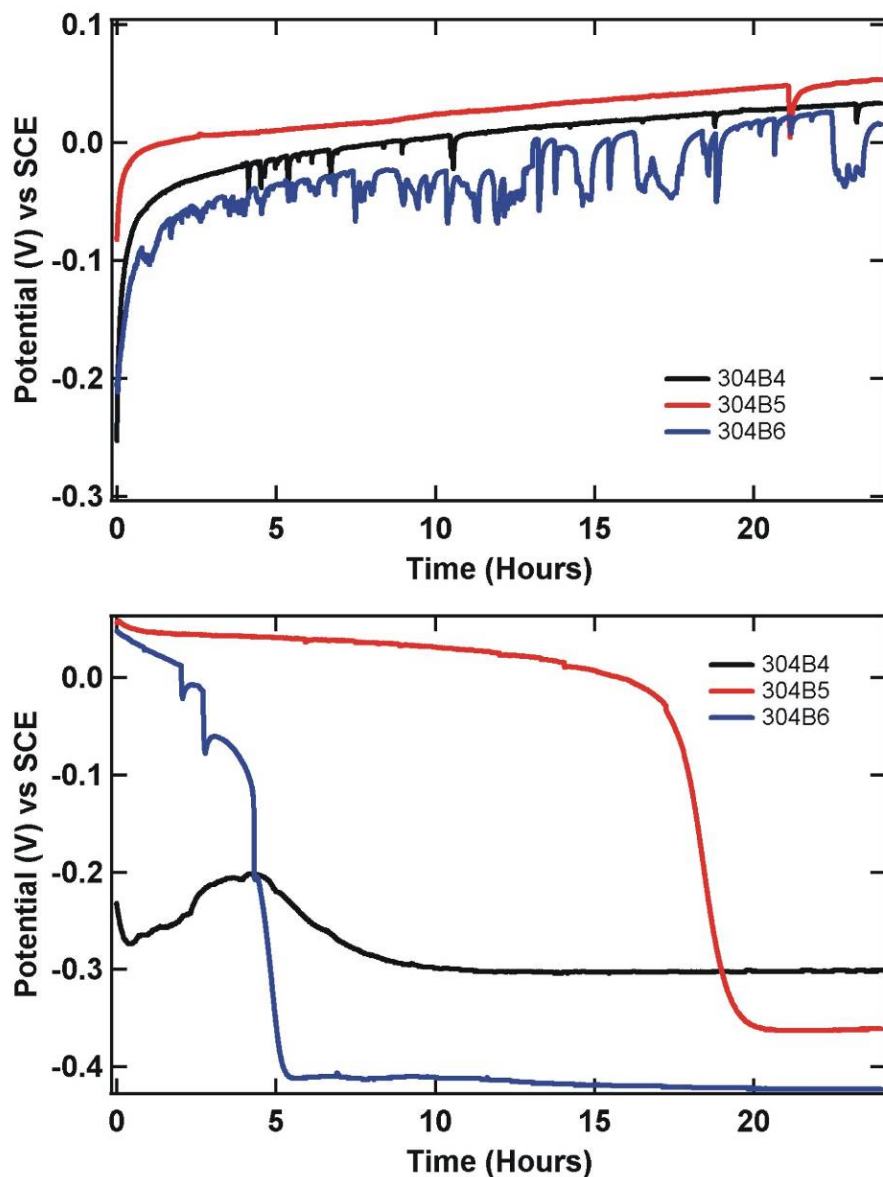
Figure 14. E_{corr} for 304B4, 304B5, and 304B6 in solution B3 at 60ºC with air (top) and N_2 (bottom) purge.

The LPR calculated corrosion rates under N_2 purge were determined using three curves. The average corrosion rates obtained from fitting were 221 ± 70 nm/yr for 304B4 (from FY-06 testing),[26] 427 ± 132 nm/yr for 304B5, and 464 ± 100 nm/yr for 304B6.

The PS curves for the three Neutrosorb Plus alloys are shown in Figure 15. The alloys with lower boron content (304B4, 304B5) show passivation during the test while the 304B6 shows much higher current, particularly at the end of the test where crevice corrosion was observed. This specimen was coated with a thick iron-oxide film. While small pits were observed under the MCA crevice formers, the most significant corrosion was observed at the Teflon compression fitting used to isolate the specimen electrical contact. One PS experiment was performed for 304B5 with Teflon MCA washers at 0.1 V versus SCE. Figure 16 shows significant current increase initiated during the test that was consistent with crevice corrosion under the MCA in post-test inspection.

Figure 15. PS curves for 304B4, 304B5, and 304B6 in solution B3 with ceramic MCA.

Figure 16. PS curve for 304B5 in solution B3 with Teflon MCA.

3.2.7 Additional PS Testing for Nickel-based Alloys at 90°C

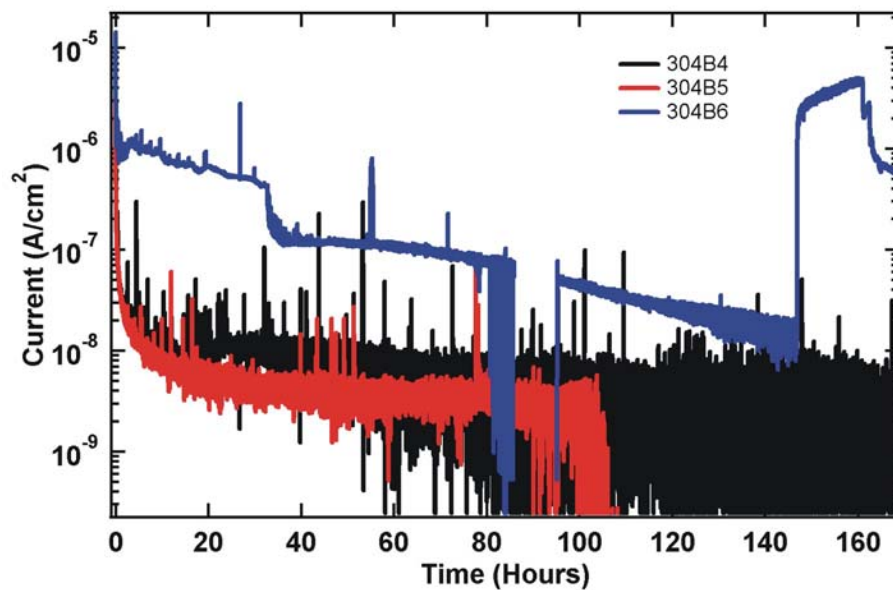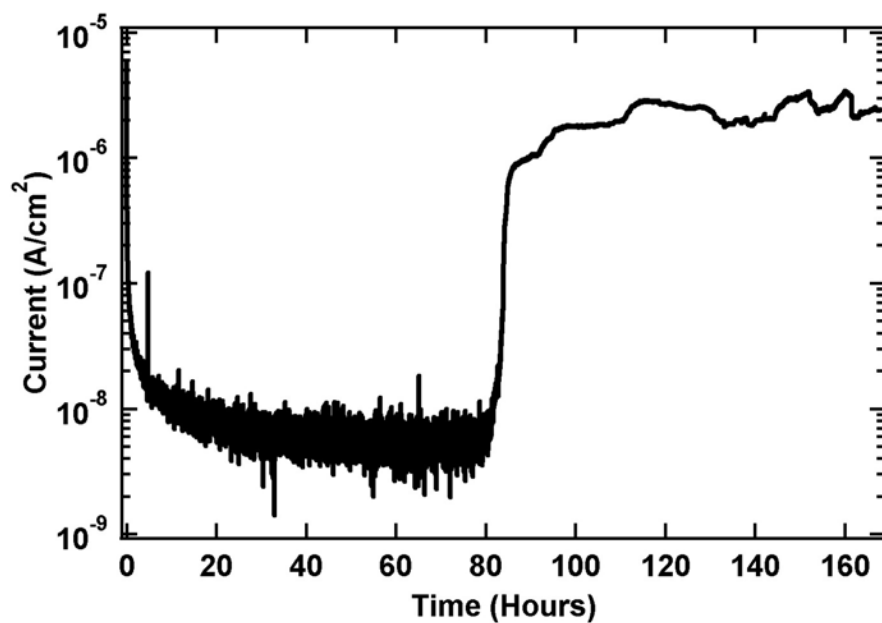Data from the electrochemical tests is shown in Table 9. The E_{corr} was greatest for the Alloy 22 specimen and somewhat lower for the Ni-Cr-Mo-Gd alloys. The total charge was much higher for the M340 alloy (lowest chromium level), with Alloy 22 having the lowest overall charge passed during the test. From the final value of the PS tests, the corrosion (I_{corr}) rate was calculated. This approach can have some error due to the random fluctuation in the corrosion current due to crevice corrosion events. A value of the corrosion rate based on the weight loss during the test is also calculated. Figure 17 shows a plot of the current for these three alloys. The Alloy 22 specimen showed the highest passivity at the early stages of the test. However, at later times, crevice corrosion was initiated and an increase in the current to levels similar to the Ni-Cr-Mo-Gd were observed.

Table 9. Data from electrochemical tests (Ni-based alloy tests).

Alloy	E_{corr} (V)	Total Charge (C/cm^2)	I_{corr} (A/cm^2)	I_{corr} CR (μm/yr)	Weight Loss (mg)	CR from gravimetric analysis (μm/yr)
M340	-0.4409	3.22	3.39E-06	34.3	12.62	47.2
M327	-0.4468	1.37	1.07E-06	10.4	5.46	19.6
Alloy 22	-0.3962	1.12	2.08E-06	20.2	4.11	15.7
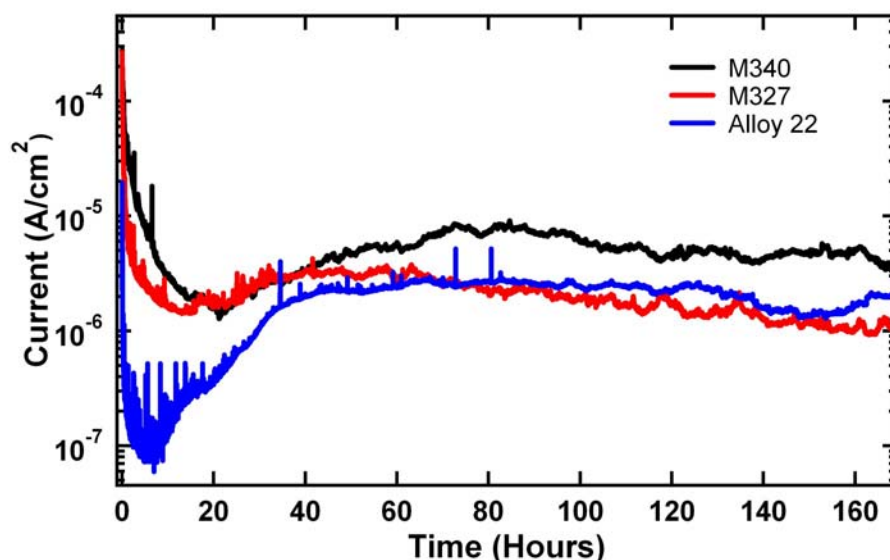
Figure 17. Current traces during PS tests.

3.2.8 Post-Test Analysis of PS Test Specimens

After the tests, analysis of the specimens and test solutions involved visual inspection, gravimetric analysis, LOM, and SEM. Table 10 provides brief post-test observations for the 304B4 and Ni-Cr-Mo-Gd specimens. The solutions were clear and colorless, except for Test 082106 where the reference electrode failed, resulting in unknown potentials (transpassive corrosion). This solution was yellow from dissolved

chromate ions. The specimens were free of extensive damage to the surface and were shiny, with evidence of slight hazing due to secondary-phase removal for the Ni-Cr-Mo-Gd specimens (see Figure 18). Some of the Ni-Cr-Mo-Gd specimens showed staining under the crevice former as a result of gadolinide removal.

Table 10. Post-test PS test observations.

Test ID	Alloy	Solution	Solution Observations	Specimen Observations
072406	304B4	B1	Clear and colorless	One small crevice pit
072506	304B4	B3	Clear and colorless	Light pitting under several crevice formers
072606	304B4	B1	Clear and colorless	one crevice area (etched)
080806-1	304B4	B1	Clear and colorless	Etching under several crevice formers
080806-2	304B4	B1	Clear and colorless	Etching and pitting under several crevice formers
080906-1	304B4	B3	Clear and colorless	No crevice corrosion
081406	Ni-Cr-Mo-Gd	B1	Clear and colorless	Partial surface gadolinide removal
081706	Ni-Cr-Mo-Gd	B3	Clear and colorless	Partial surface gadolinide removal
082106	Ni-Cr-Mo-Gd	B1	Clear and yellow	Heavy etching on boldly exposed surface, removal of surface gadolinides
082406	Ni-Cr-Mo-Gd	B3	Clear and colorless	Partial surface gadolinide removal

Representative LOM images of the damage from each of these alloys are shown in Figure 18. In several cases, small pits or light etching was observed under a crevice former for 304B4 specimens (see Figure 18). The most damage was observed for Tests 080806-1 and 080806-2, which were incomplete and are not shown. For the Ni-Cr-Mo-Gd tests, the removal of the gadolinide phase was partial for completed tests (Tests 081406, 081706, 082406). No evidence of primary phase corrosion was found for the Ni-Cr-Mo-Gd alloys. Figure 19 shows that there was a partial removal of the gadolinide secondary phase for Test 081406.
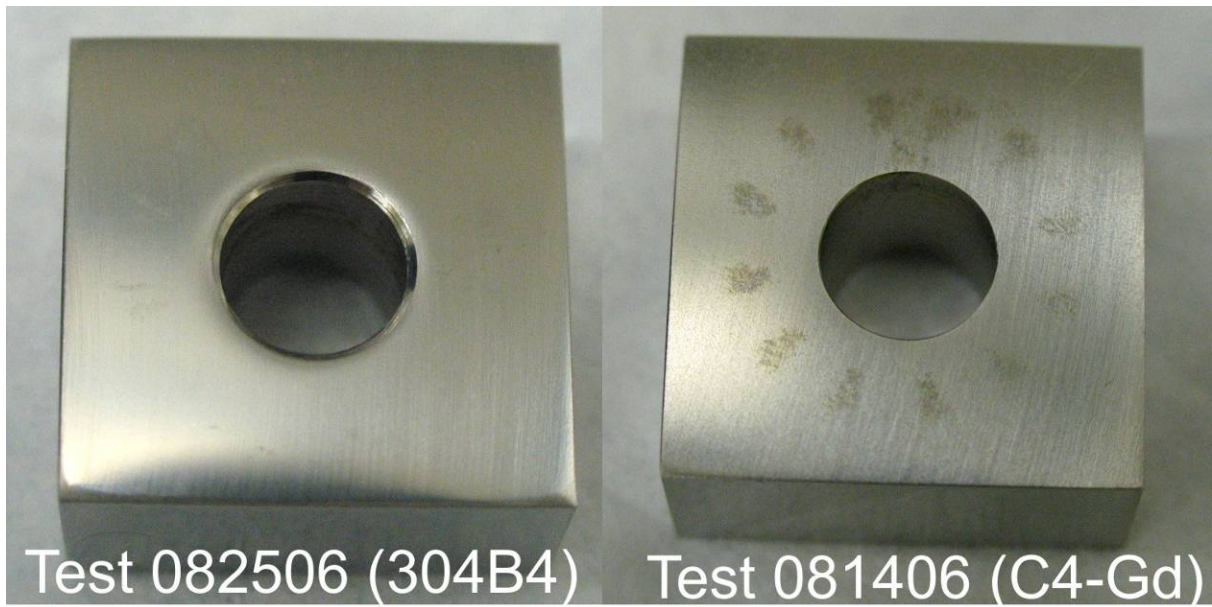
Figure 18. Photographs of PS test specimens after testing.
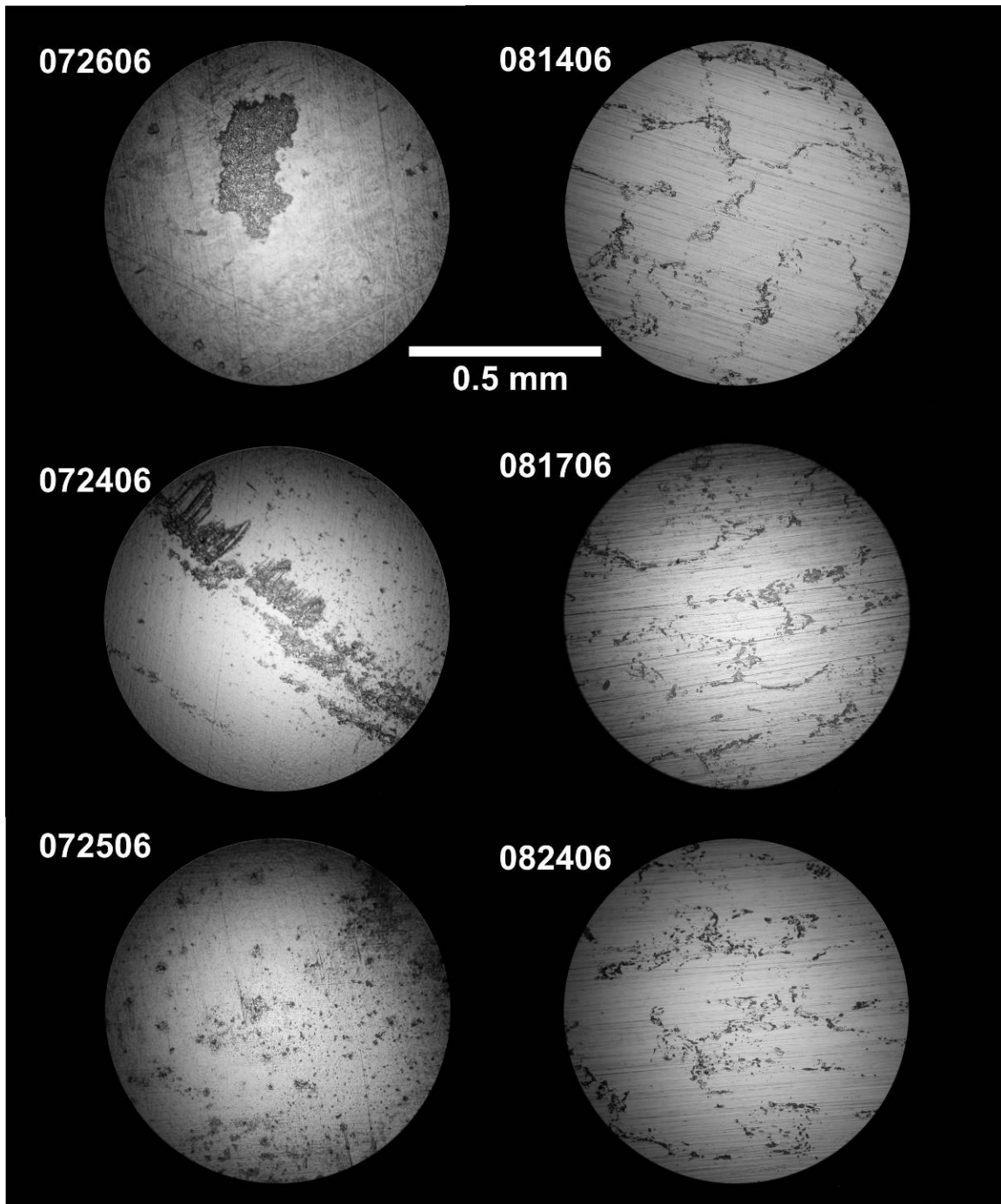
Figure 19. LOM images of selected specimens showing damage to the surface. Tests 072606, 072406, and 072506 are 304B4 specimens, and Tests 081406, 081706, and 082406 are Ni-Cr-Mo-Gd specimens. All images were taken at a magnification factor of 200×.

The specimen surfaces were also observed with SEM in both secondary electron (SE) and backscatter electron (BSE) modes. Images of 304B4 are shown in Figure 20. Figure 20A shows a large shallow area of damage while the other images are of smaller pits, less than 100 µm in size. The BSE images show the numerous Cr_2B phases (darker grey) in the material. The darker areas are corrosion sites or accumulated

scale. Figure 21 shows the Ni-Cr-Mo-Gd alloy after corrosion testing. The bright areas are due to the gadolinide phase particles, which appear to be partially removed. Figure 21C shows the area of an entire MCA tooth where the gadolinide under the tooth is removed while the surrounding material is still intact. Figure 21A and B shows the edge of the crevice former where the inner gadolinides are removed, while gadolinides outside the crevice appear intact.
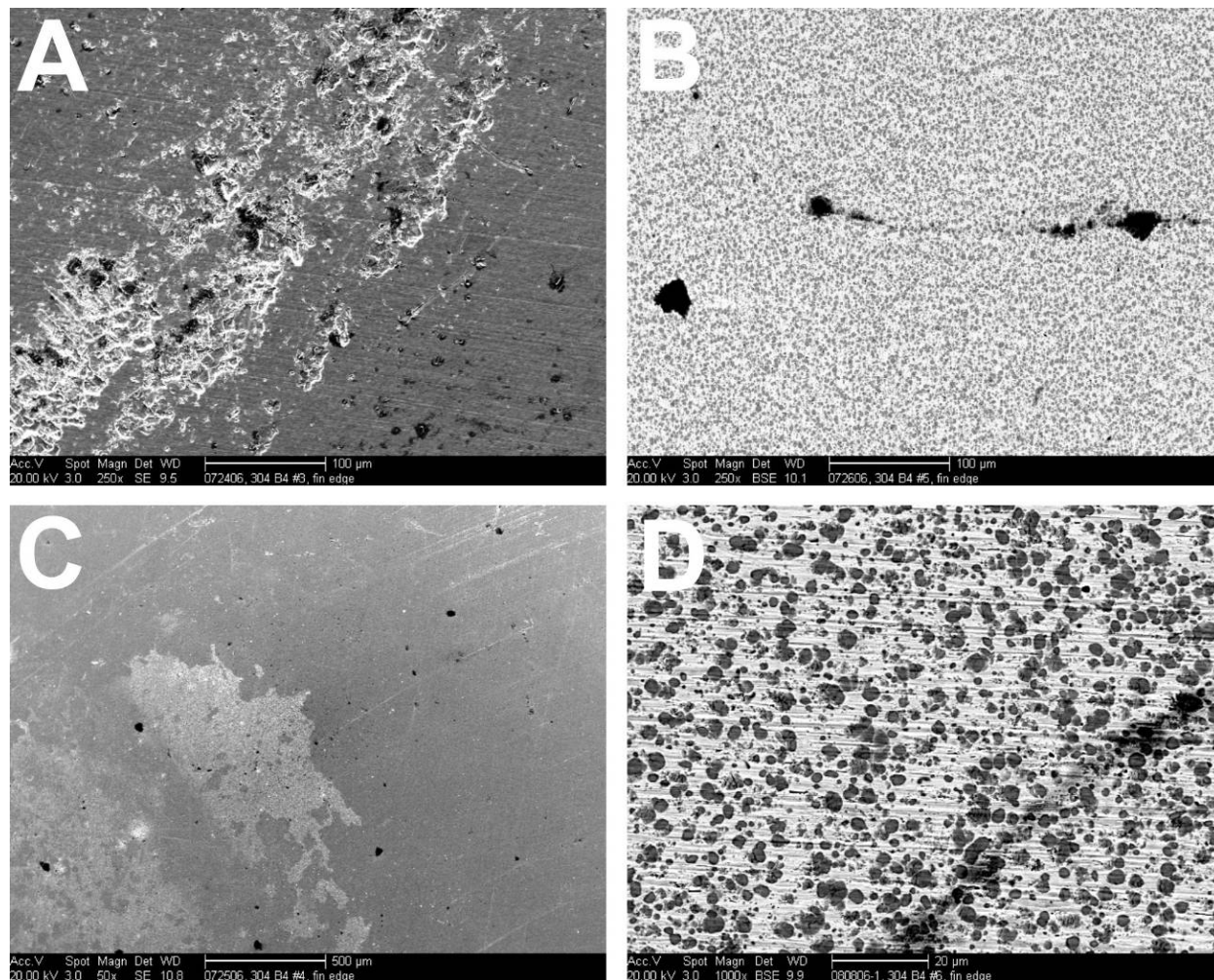
Figure 20. Scanning electron microscopy (SEM) images of 304B4 alloy corrosion specimens following testing. The images were obtained in SE (A and C) and backscatter electron (BSE) (B and D) modes.
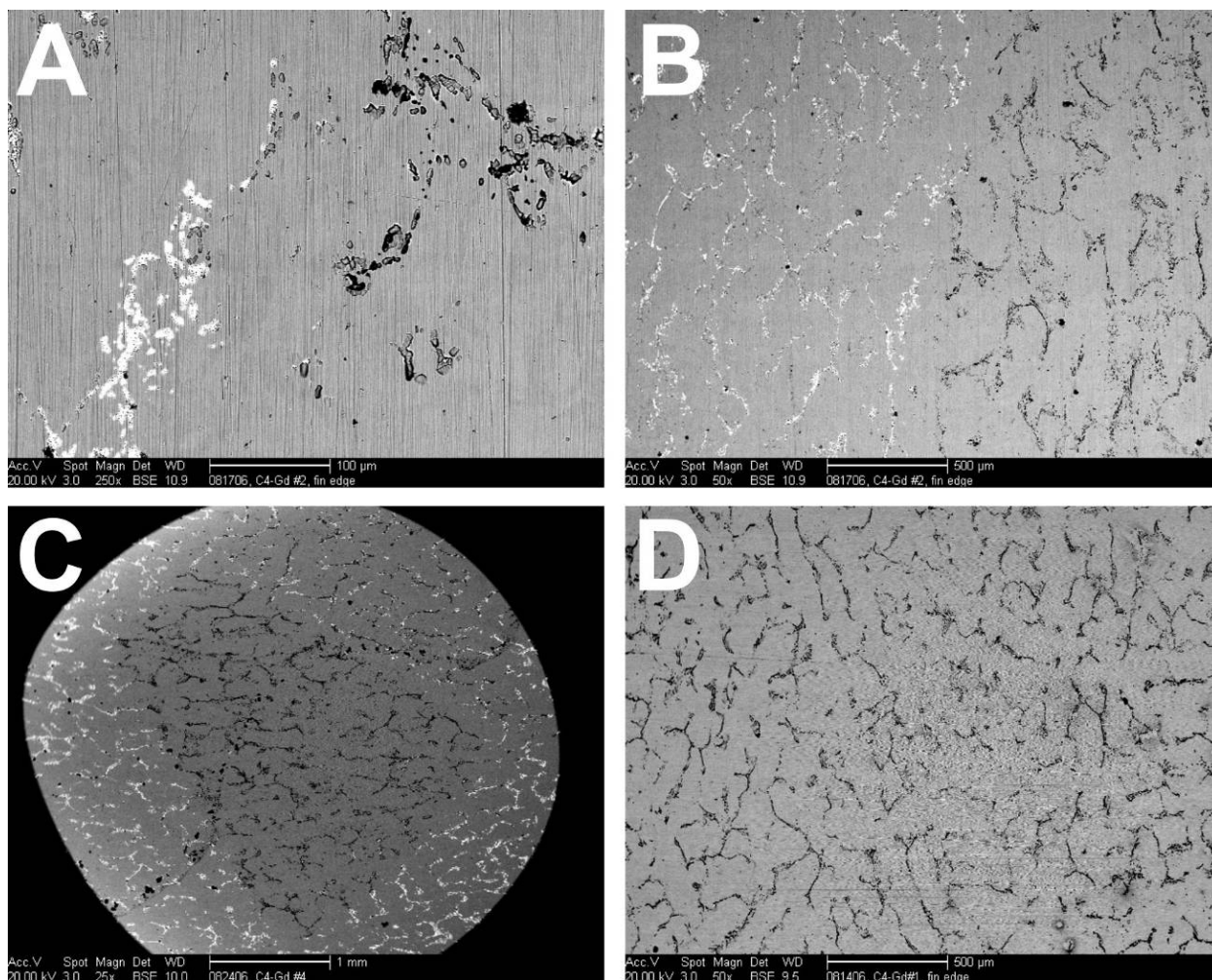
Figure 21. SEM images of Ni-Cr-Mo-Gd alloy corrosion specimens following testing. The images were obtained in BSE mode.

Additional SEM work was performed to show the microstructure of the secondary phases after testing. The SEM images were obtained in BSE mode to enhance the contrast of the secondary phase. Figure 22A and B shows the microstructure of the A978 alloy (Test 080206), with large secondary-phase particles compared with the 304B4 specimen (Test 080806-1), having smaller, more evenly distributed secondary-phase particles. The SEM image of the Ni-Cr-Mo-Gd specimen from Test 082406 shows the partial removal of the gadolinide phase. Small cavities remain from particles that were dissolved. No evidence of localized corrosion damage extending beyond these cavities was found.
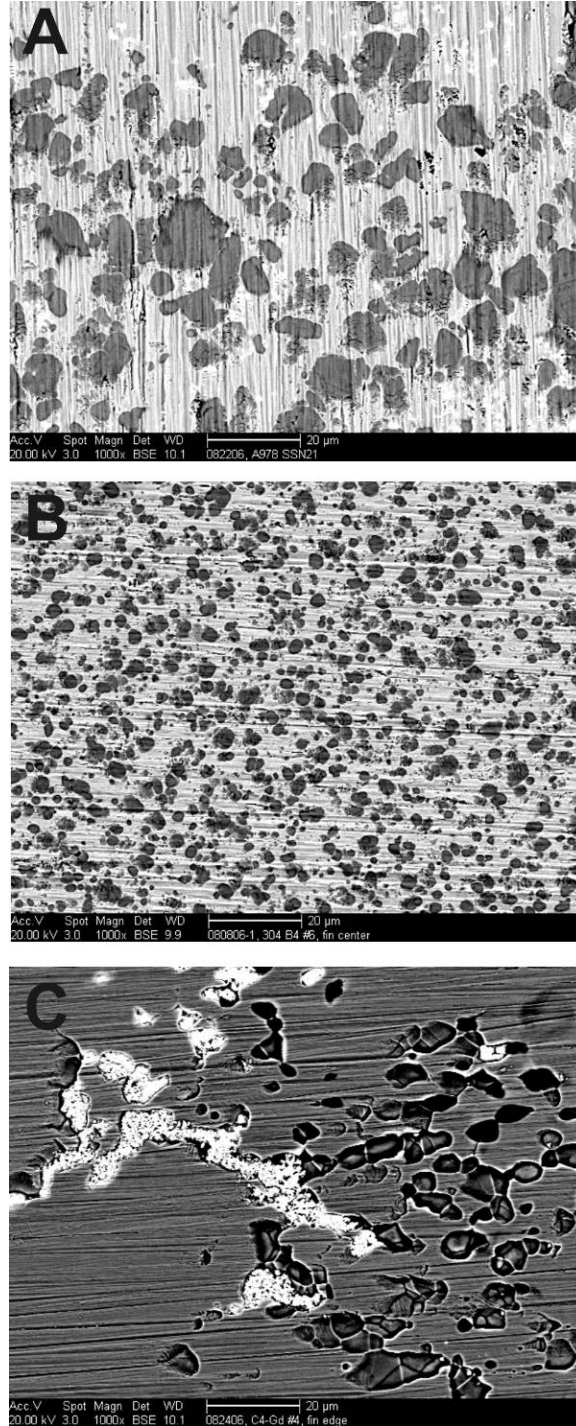
Figure 22. SEM images obtained in BSE mode showing the secondary phase particles for (A) A978, (B) 304B4, and (C) Ni-Cr-Mo-Gd alloys.

3.2.9 Post-test Analysis of Alloy 22 and Ni-Cr-Mo-Gd Test Specimens

Figure 23 shows photographs of the specimens after descaling. All the specimens show a similar amount of damage and number of crevice corrosion sites attacked. There was a difference in the amount

of crevice corrosion from one side to the other. This is likely due to the N_2 purge affecting the chemical transport, with the side most affected having less crevice attack. There are some differences in the attack of the Ni-Cr-Mo-Gd alloys versus Alloy 22. The Alloy 22 attack was more at the edges of the crevice tooth, while the Ni-Cr-Mo-Gd is more uniform across the crevice tooth. There is more pronounced staining of the Alloy 22 specimen.
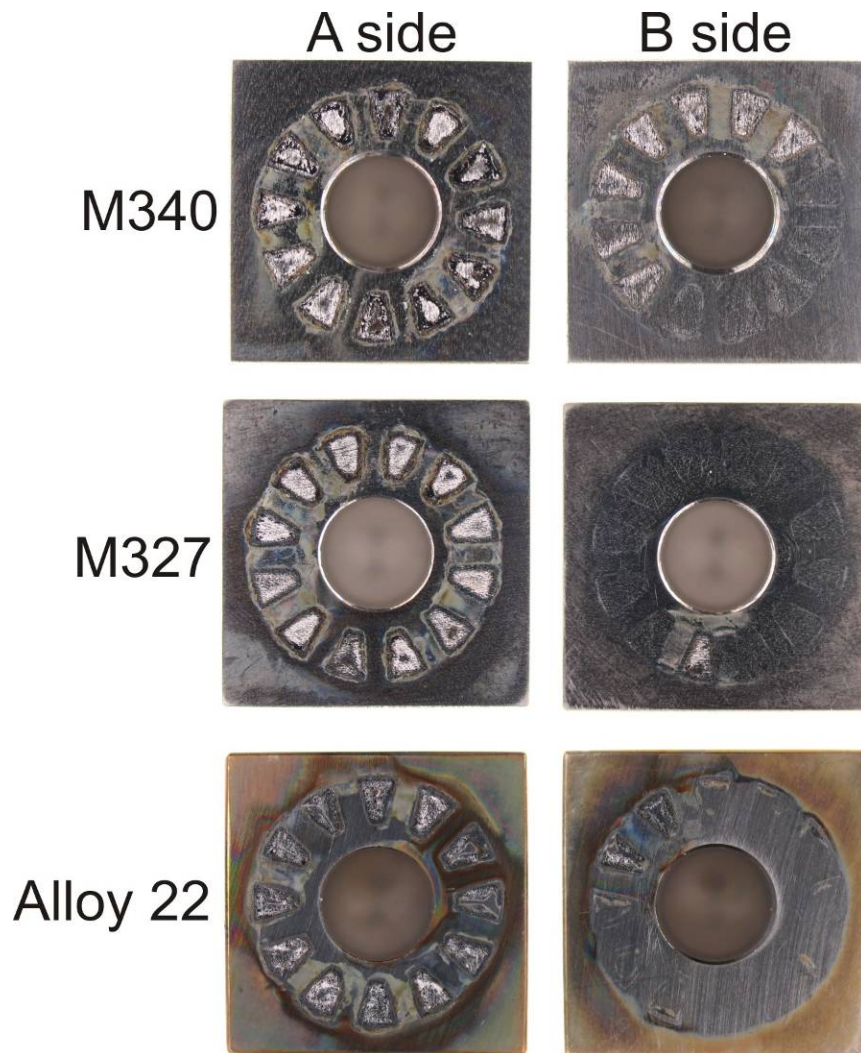
Figure 23. Macro photographs of the three alloys after descaling. The most damaged side is in the "A" column, and the less damaged side is in the "B" column.

3.2.10 Post-Test Analysis of Borated Stainless Steel Using an Optical Profilometer

Figure 24 shows optical profilometer data acquired on Neutrosorb Plus 304 stainless steels after corrosion testing. Figure 24A shows the extensive crevice corrosion damage to 304B6 at the Teflon compression gasket during exposure to solution B3 at 60ºC at E_{corr}. Figures 24B and C show damage from a PS test for 304B4 under the Teflon MCA. Figure 24B shows what appears to be removal of material around secondary-phase particles in what could be the initiation of localized corrosion. Figure 24C shows the edge of a crevice corrosion pit where islands of material, on the same level as the polished surface, remain. These islands are likely secondary-phase particles (borides) that had not been released from the surface as the stainless steel austenite matrix was etched around them.

Figure 24. Optical profilometer data of specimens after corrosion experiments. (A) is 304B6 after E_{corr} measurement for 4 weeks in solution B3, and (B) and (C) are the 304B4 specimen damage from under the Teflon crevice former after the PS test at 0.1 V in solution B3.

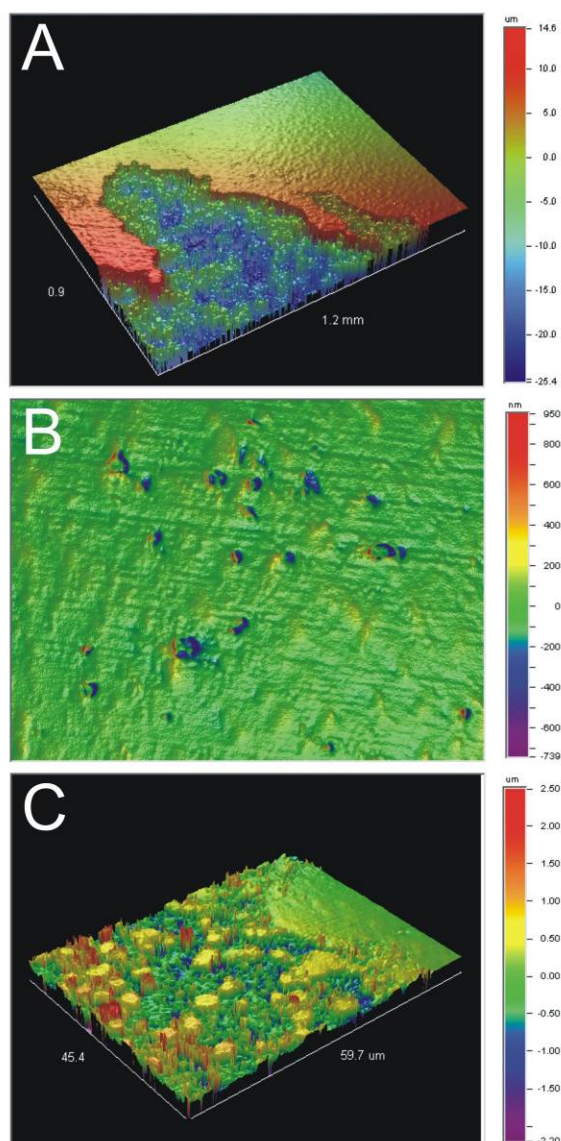# 4.   CORROSION PRODUCT ANALYSIS

4.1.1   Corrosion Product Analysis of Grade A Borated Stainless Steels

Prior work has identified the composition of the borides found in Grade A material to be a Cr_2B type with a composition in weight percent of Cr-46, Fe-40, Mn-3.5, Ni-1.0 and B-9.5 and a compound formula of $(Cr.53.Fe.42.Mn.04.Ni.01)_2B$.[10] Reported results for Grade B ingot-metallurgy material identify the borides as a M_2B type where M is a metal[27] with a chromium level of approximately 50% and iron at about 40%. Analysis performed at Bohler Bleche identifies the borides as $(Fe,Cr,Ni,Mn,Mo)_2(B,C)$.[28] The higher chromium level in the borides will deplete the base metal austenite next to the boride of this element.[9]

There was no evidence of a corrosion product detected on the surface of any of the Grade A borated stainless steel specimens in the testing program. As discussed in Section 3.2.5, the only damage was observed at the electrical connection point under the Teflon gasket. Representative images of the damage in this area are shown in Figures 25 and 26. The particles are the chromium-rich borides, and the corrosion mechanism appears to be localized corrosion around the borides, which allows them to fall free from the surface. The test solutions were filtered to gather a sample for XRD analysis, but the measurement results were inconclusive due to a very small sample size.
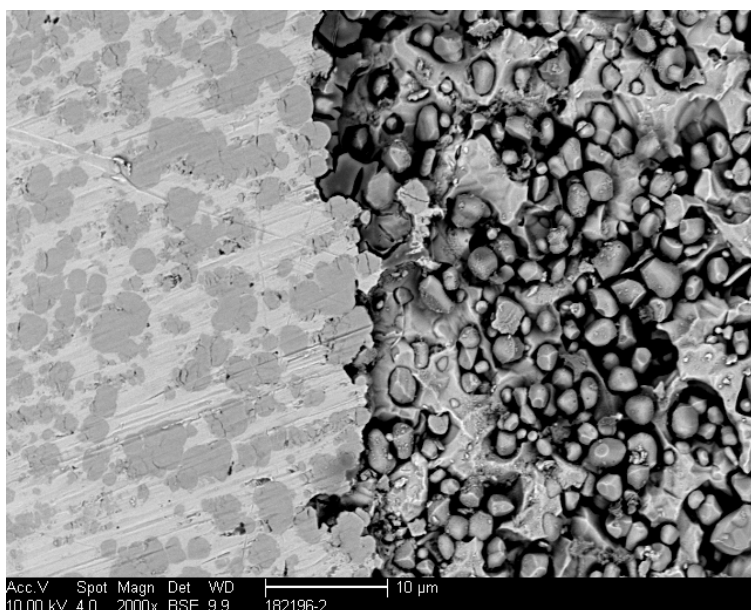

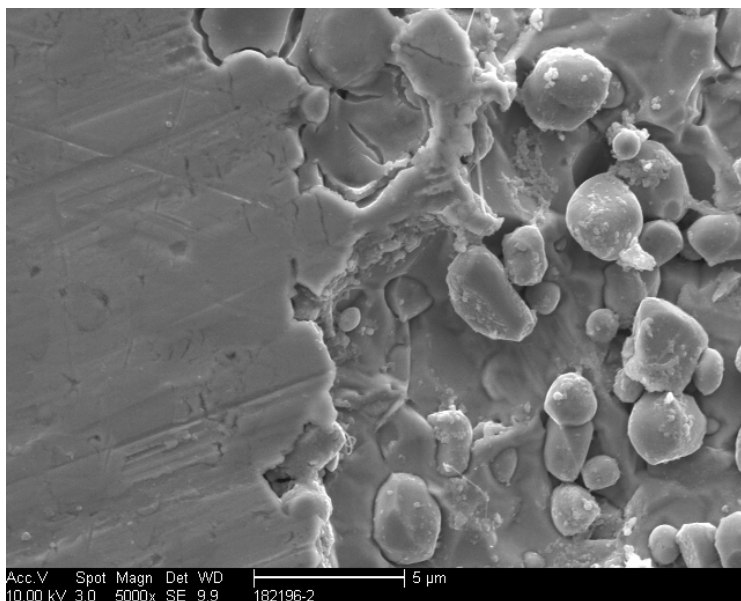Figure 25. BSE image of localized corrosion near gasket in 304B6.

34

Figure 26. Secondary electron (SE) image of localized corrosion near gasket in 304B6.

4.1.2   Accelerated Corrosion Product Study

To increase the amount of corrosion product for XRD analysis, an accelerated corrosion test was performed using a 304B6 crevice-corrosion specimen polarized above the expected E_{corr} value (0.4 V versus SCE) at 90ºC for 24 hours in solution B3. The 304B6 alloy was chosen as it shows a reduced resistance to localized corrosion compared to alloys 304B4 and 304B5 as reported in Section 3.2.6. This resulted in an excessive amount of crevice corrosion product that clouded the solution significantly (see Figure 27) and resulted in catastrophic attack to all surfaces of the specimen. The precipitate and corrosion product on the specimen was black and mostly lacked additional color. A total charge of 5616 C (355.4 C/cm^2) was passed during the test, with a maximum current of 5.29 A/cm^2 and a minimum of 2.25 A/cm^2. Thus, localized corrosion was initiated instantly and remained active throughout the test. The specimen lost 1.83141 g during the test. Precipitate was collected during descaling, with sonication in 10% HNO_3. After descaling cleanup, the specimen continued to produce small grey particles upon shaking. The particles from descaling were analyzed by XRD and matched with $FeCr_2B$. A similar match was made with settled precipitate collected at the bottom of the flask, which also indicated significant amounts of amorphous material.
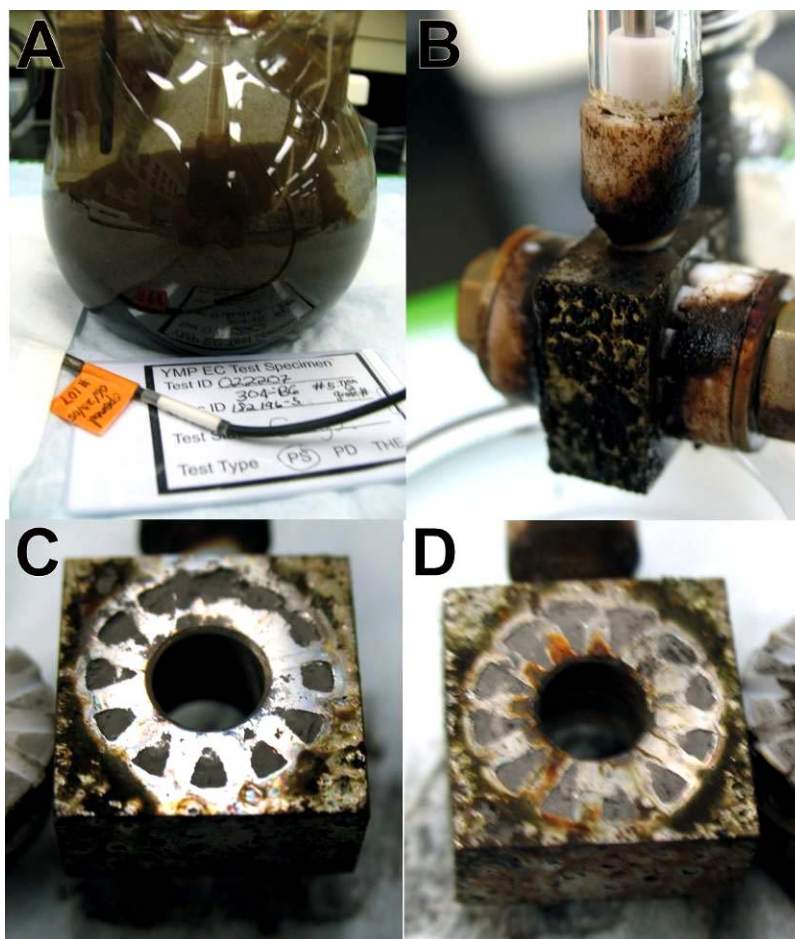
Figure 27. Photographs of corrosion damage from 304B6 specimen in accelerated test: (A) corrosion flask, (B) specimen immediately after removal, and (C) and (D) two sides of specimen.

4.1.3 Neutronit Sample SSE 30 from the LTCTF

To further analyze the corrosion products that are evolved from the surface of a borated stainless steel undergoing localized corrosion, an examination was made on sample SSE-30, a Neutronit A978 sample (Heat E084295 in Table 1). This specimen was exposed at the water line to simulated cement modified water (SCMW) at 90°C for 2,134 days at the Long Term Corrosion Test Facility (LTCTF), formerly located at LLNL. [13,29]

The specimens in the test program were affixed to an insulated and threaded rod through a central hole, as shown in Figure 28.[29] Note that part of the test specimen is cut away in the drawing for clarity. The specimens are held apart by Teflon spacers. The weight-loss specimen test assembly is fastened to a test rack, which is inserted into the large corrosion test vessels, as shown in Figure 29.
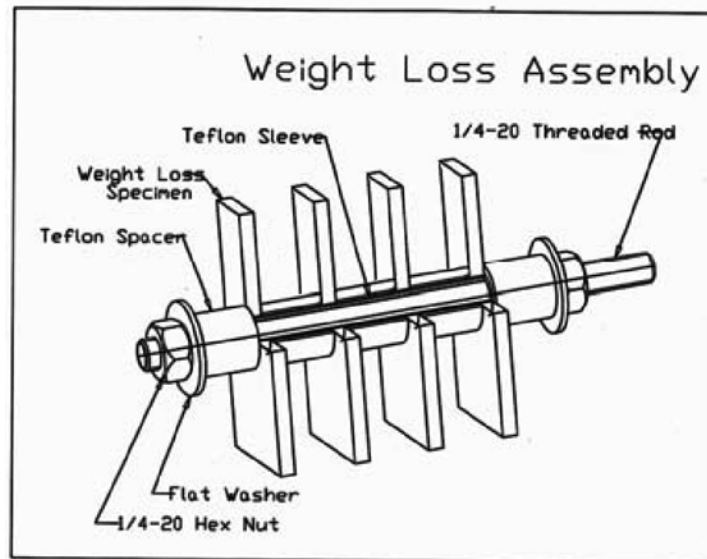
Figure 28. Weight loss assembly at the Long Term Corrosion Test Facility (LTCTF).[29]

**Weight loss
specimens**
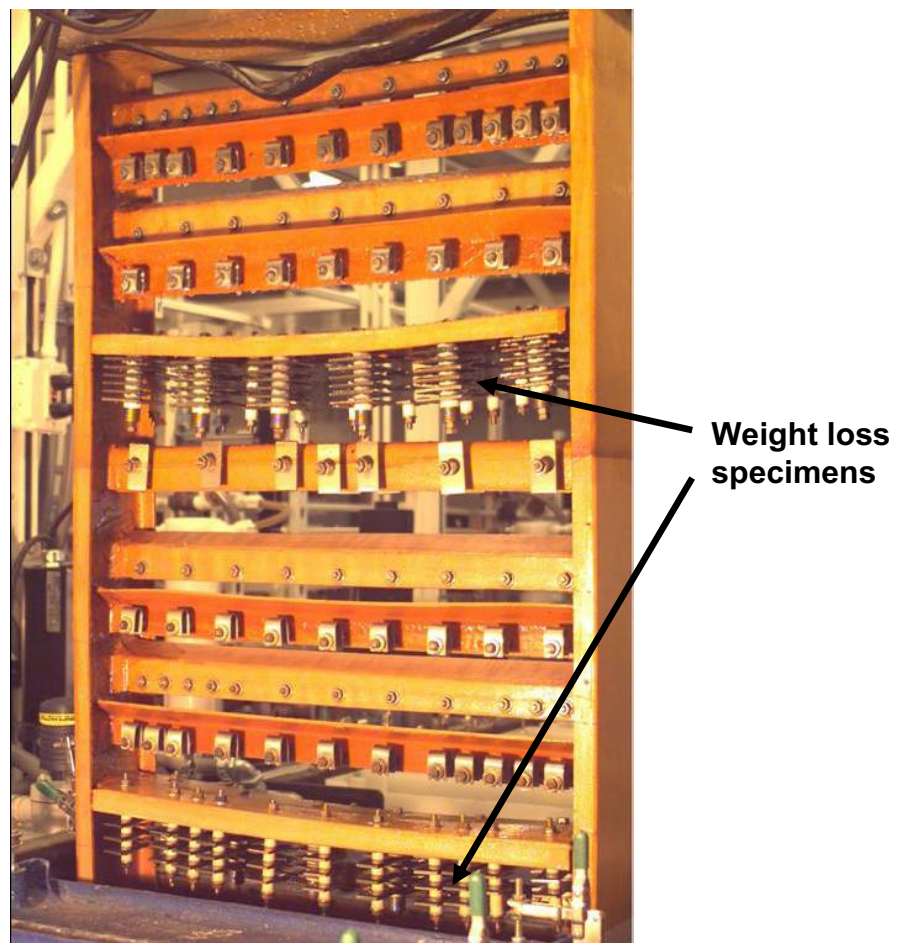
Figure 29. Typical LTCTF corrosion test rack.[29]

For preparation of the sample for analysis, an area with a large corrosion product cap on the surface was chosen, and the cut was made through this area, which is marked by the red line in Figure 30. This surface corrosion product was located under and adjacent to a Teflon washer as described in the experimental procedure section of the LLNL corrosion paper. Figure 30 shows the area of the test specimen that was prepared for analysis.
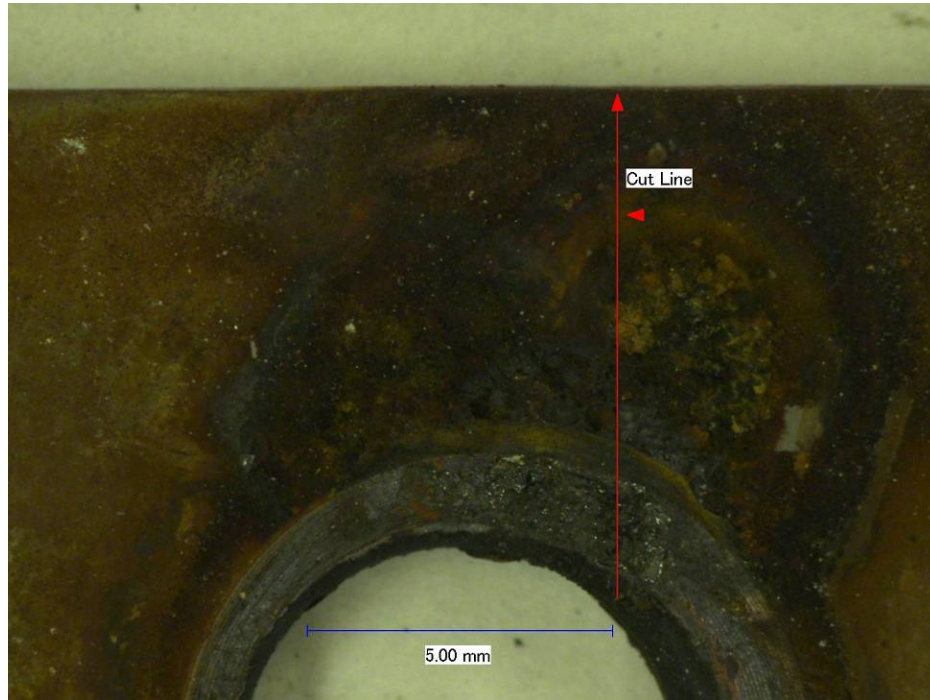
Figure 30. Specimen SSE 30 cut line.

LOM images of the specimen after vacuum mounting are shown in Figures 31 and 32. The sample is totally penetrated under the Teflon attachment washer, with corrosion products evident on the surface and under the original surface.
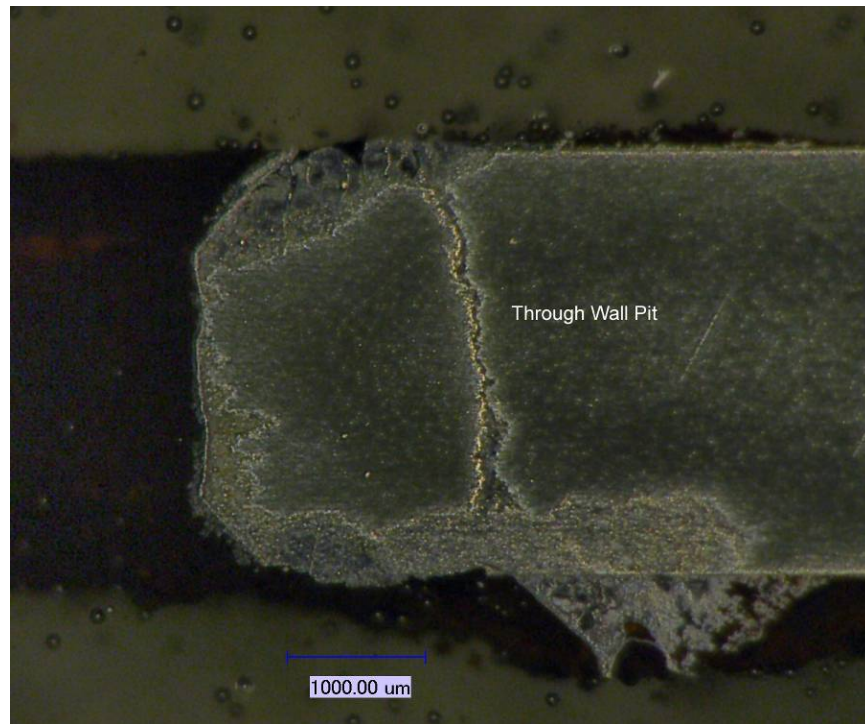
Figure 31. Specimen SSE 30, mounted specimen, showing through-wall penetration and corrosion product.
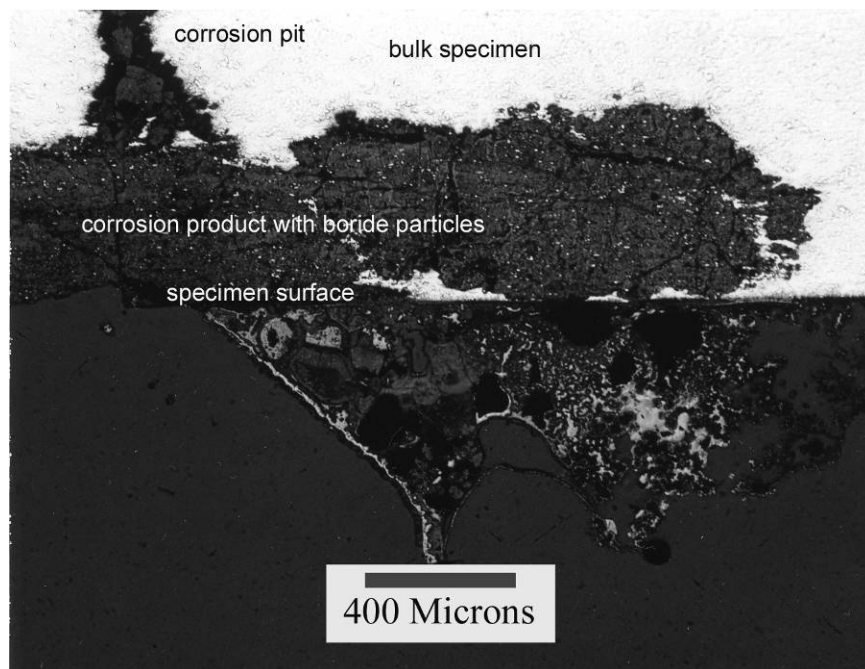
Figure 32. Specimen SSE 30 corrosion products.

Figure 33 shows a SEM SE image of the sampling areas for the corrosion products that lie above and below the original sample surface.
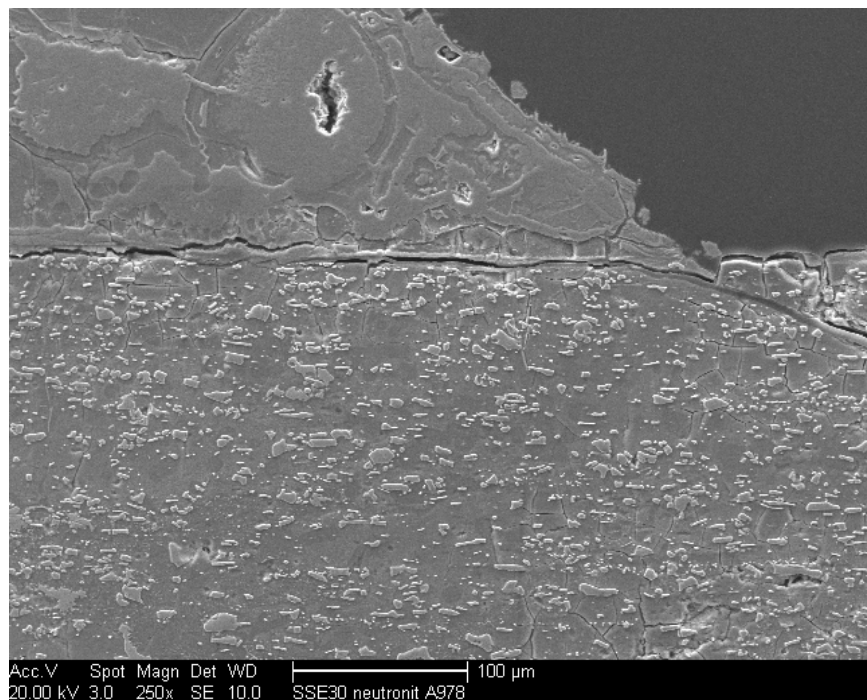
Figure 33. Specimen SSE 30 SE image.

As shown in Figure 34, an area was chosen (box with black border) for sampling in the corrosion product found under the apparent original sample surface. The analytical results are in Table 11. The particles, marked as spots 1 and 2, appear to be borides. Spot 3 has the physical appearance of a boride, but no boron was detected. Spots 4 and 5 are corrosion products where some boron was detected in spot 4 and no boron was detected in spot 5.
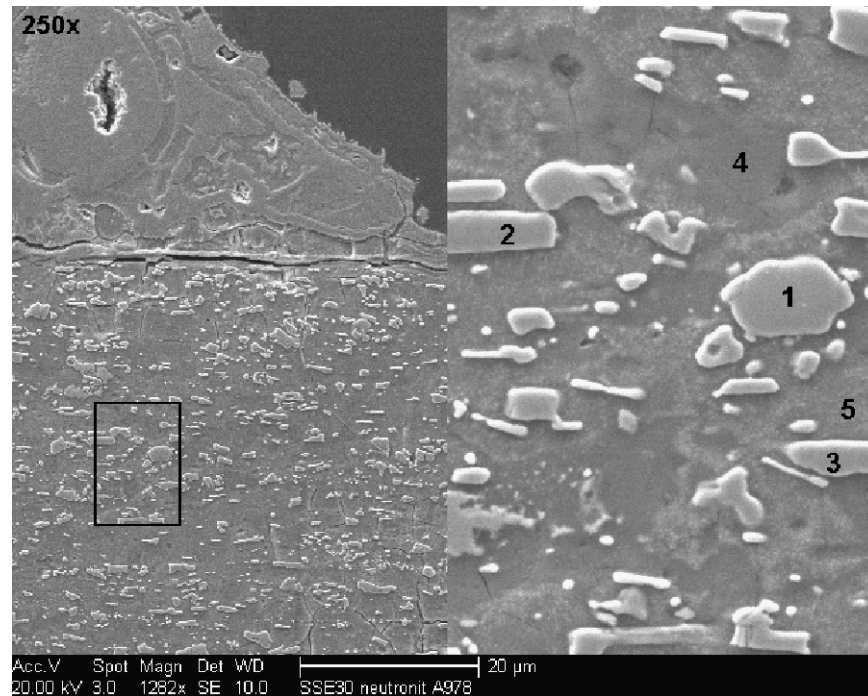
Figure 34. Specimen SSE 30 SE image, corrosion product analysis. (The 20 μm bar corresponds to the image on the right.)

Table 11. Corrosion product analysis, below original surface.

Element	Spot 1	Spot 2	Spot 3	Spot 4	Spot 5
B	1.84	2.02	0.00	1.32	0.0
C	0.62	0.70	0.00	0.99	0.68
O	2.81	2.74	2.67	32.72	37.43
Mo	2.93	2.80	3.06	14.20	13.87
Cr	47.25	48.56	49.85	38.96	38.05
Mn	0.98	1.15	1.24	0.24	0.16
Fe	42.76	41.22	42.16	6.68	4.85
Ni	0.80	0.81	0.97	4.15	3.94
Cu	0.00	0.00	0.06	0.75	1.04

The sample area shown in Figure 35 is the corrosion product deposited above the apparent original-sample surface. The analysis results of the sampled areas are shown in Table 12. The sample areas are iron and chromium-corrosion-product oxides in which boron was detected. Boron was found in the four sampled areas of the corrosion product found on the sample surface.
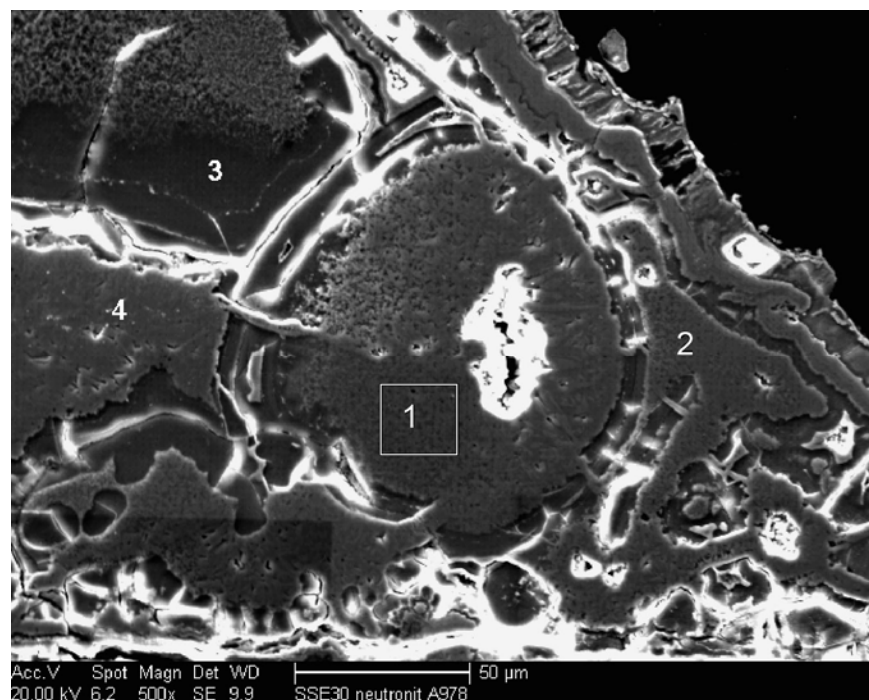
Figure 35. Specimen SSE 30 SE image, corrosion product analysis.

Table 12. Corrosion product analysis, above original surface.

Element	Spot 1	Spot 2	Spot 3	Spot 4
B	2.72	1.31	3.94	1.98
C	1.75	1.24	1.74	1.15
O	31.27	29.90	29.09	30.69
Mo	2.36	6.15	4.88	2.60
Cr	6.91	7.72	50.37	1.68
Mn	0.61	0.70	2.90	0.31
Fe	52.40	52.07	3.74	58.43
Ni	1.86	0.80	3.16	3.01
Cu	0.12	0.11	0.19	0.16

An area of the bulk metal (unetched) below the corroded surface is shown in Figure 36. The analysis results for the sampled areas are shown in Table 13. The secondary-phase particle sampled at spot 1 is a boride, and spots 2 and 3 correspond to the chemistry of the base austenitic structure of this alloy. Spot 3 does identify boron, but this value may be from borides adjacent or underneath the sampled area being measured by the beam.
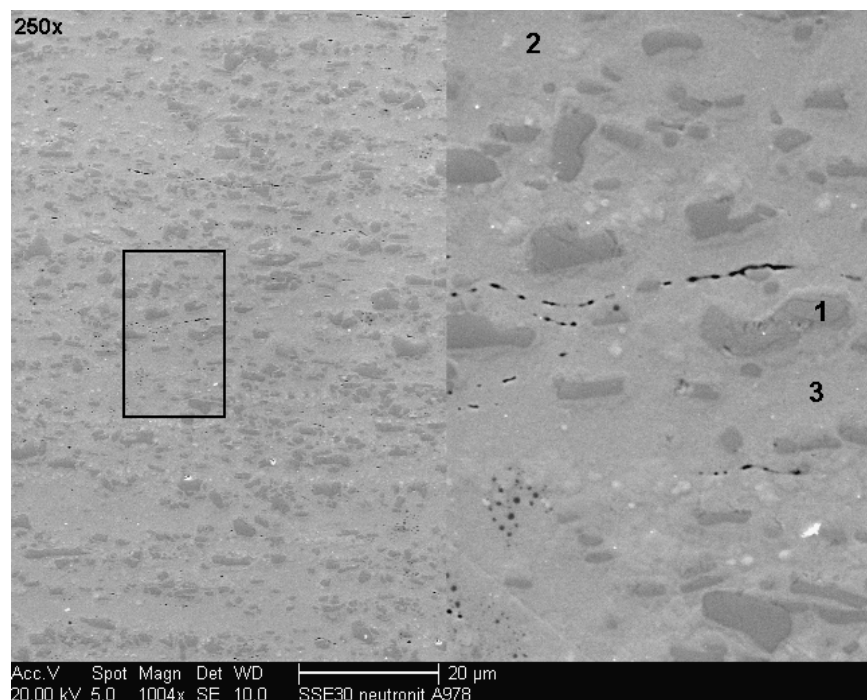
Figure 36. Specimen SSE 30 SE image, bulk metal boride analysis. (The 20 µm bar corresponds to the image on the right.)

Table 13. Specimen SSE 30, bulk metal analysis.

Element	Spot 1	Spot 2	Spot 3
B	2.47	0.00	1.67
C	1.49	0.38	0.75
O	2.77	1.41	1.40
Mo	4.58	1.68	1.53
Cr	39.25	11.22	11.07
Mn	3.99	2.25	2.09
Fe	38.53	68.67	67.62
Ni	3.28	13.52	13.32
Cu	3.65	0.87	0.55

4.1.4   Analysis of Corrosion Product from Neutronit Specimen SSE2 from the LTCTF

A loose sample of the corrosion product in the storage bag of sample SSE-02 was collected and analyzed by XRD. Sample SSE-02 is a Neutronit A978 sample (Heat E084295 in Table 1), which was exposed in the vapor space to simulated acidified water at 90°C for 2,134 days at the LTCTF.[13] The results show that the corrosion product consists mainly of $FeO(OH)$ (goethite) and Fe_2O_3 (hematite) with no evidence of crystalline borides being present.

5. CONCLUSIONS

Corrosion testing of five neutron-absorbing alloys, Type 304B4 Grade A, Type 304B5 Grade A, Type 304B6 Grade A, Neutronit A978, and Ni-Cr-Mo-Gd alloy, was performed using electrochemical testing methods. One test sequence compared the performance of two different heats of a Ni-Cr-Mo-Gd with the Ni-Cr-Mo alloy specified for the waste package outer barrier (Alloy 22).

The conditions were based on those expected for a waste package, should the outer barrier breach and the internals be exposed to moisture. PD tests were performed to determine the localized characteristics of the materials. Measurement of the E_{corr} was used to determine the equilibration potentials under aeration to determine values for performing PS tests. The PS tests hold the potential of the specimen at a value, as determined from the E_{corr} testing while measuring the current. The current from this test can be used to determine the corrosion rate and/or propensity toward localized corrosion. In addition, LPR tests were performed as a second method to determine the corrosion rate. Damage to the specimens was observed using photography, LOM, and SEM.

While acceptable results were obtained for 304B4 and Ni-Cr-Mo-Gd alloys, experimental problems occurred for the A978 alloy in PS tests. These problems stemmed from having to adapt long-term exposure test specimens to electrochemical testing. The problem was due to the method used for specimen contact.

The testing performed on these neutron absorbers has shown behavior that contradicts some of the previous work on these types of alloys.[13,30] However, in those previous tests the conditions are more aggressive (temperature, pH, ionic content, etc.) than those used here. The tests here contain very low ionic contents and/or moderate pH values, as defined in the Technical Work Plan.[19] Very passive conditions were observed for the 304B4 SS in all cases. There was evidence of metastable pitting on the borated stainless steel, though sustained pitting events were not observed. Several 304B4 specimens showed significant but isolated damage under the crevice formers. It is difficult to determine if the corrosion occurred prior to the PS tests, particularly during aeration where the potentials were fairly positive on the specimens that may not yet have been fully passivated. Some further investigation of this observation is warranted. Ideally, the tests would extend conditions such that the localized corrosion initiation threshold in potential, temperature, and solution composition (Cl/NO$_3$ ratio, pH) are known.

The results of the Ni-Cr-Mo-Gd alloy tests, compared to the borated stainless steel alloys, are less clear. The measured corrosion current for the Ni-Cr-Mo-Gd alloy was higher than that measured for the 304 B4 stainless steels, but the current, in this case, was measuring the dissolution of the secondary phase (gadolinide) for the Ni-Cr-Mo-Gd material. Therefore, the initial corrosion rate for the Ni-Cr-Mo-Gd material is determined by the very reactive gadolinide secondary phase.[31] This apparent general-corrosion rate was several orders-of-magnitude higher than for the 304B4, Grade A material. The secondary-phase (FeCr)$_2$B of the borated stainless steel appears to be stable, likely due to the high Cr content; thus, it does not contribute to the corrosion directly. This secondary phase (boride) is known to reduce the overall localized corrosion properties due to chromium depletion from the austenite phase adjacent to the boride.[10,13,27] Evidence shows that the gadolinide phase was not fully removed in these tests; thus, the final PS corrosion current values (and calculated corrosion rate) are affected by continued corrosion of the gadolinide phase. It is anticipated that the general corrosion performance would improve after the full removal of this phase and would approach the performance level of Alloy C-4 or Alloy 22, depending on the particular chromium level of the heat being tested. As shown in previous work, the primary austenitic phase of the Ni-Cr-Mo-Gd alloy was very resistant to localized corrosion. The localized corrosion resistance benefits of the Ni-based alloy would be useful for more aggressive conditions than those that were tested in this study. In any case, long-term corrosion testing needs to be performed to verify the results of these preliminary tests.

Additional work should be performed to determine a rate for the loss of boron during localized corrosion of 304B4, Grade A stainless steels. Boride dissolution by the in-package solution or capture in a corrosion product should also be investigated further.

6.   REFERENCES

1. ASTM A887-89, "Standard Specification for Borated Stainless Steel Plate, Sheet, and Strip for Nuclear Application*,"*American Society for Testing and Materials, 2004.

2. K. Wasinger, "High Density Spent Fuel Storage in Spain-Capacity for the Entire Life," *Nuclear Plant Journal*, July-August 1993, p. 46.

3. D.G. Abbott and R.E. Nickell, "Experience with Certifying Borated Stainless Steel as a Shipping Cask Material," *1ˢᵗ International Topical Meeting on High-Level Radioactive Waste Management, Las Vegas, NV, April 1990.*

4. Waste Package Neutron Absorber, Thermal Shunt, and Fill Gas Report, B00000000-01717-2200-00227 REV 00, January 2000.

5. ASTM B932-04*, Standard Specification for Low-Carbon Nickel-Chromium-Molybdenum-Gadolinium Alloy Plate, Sheet, and Strip*, American Society for Testing and Materials, 2004.

6. DOE/SNF/REP-011, *Preliminary Design Specification for Department of Energy Standardized Spent Nuclear Fuel Canisters*, Department of Energy, Volume I - Design Specification, Revision 3, August 17, 1999.

7. Quality Assurance Requirements and Description, DOE/RW-0333P, Revision 18, DOC.20060602.0001, 10/02/2006.

8. Electrochemical Corrosion Testing of Borated Stainless Steel Alloys, INL/EXT-07-12633, May 2007.

9. H.J. Goldschmidt, "Effect of Boron Additions to Austenitic Stainless Steels Part II, Solubility of Boron in 18% Cr, 15% Ni Austenitic Steel," *Journal of the Iron and Steel Institute*, November 1971, p. 910.

10. J.W. Martin, "Effects of Processing and Microstructure on the Mechanical Properties of Boron-Containing Austenitic Stainless Steels," *Proceedings Symposium Waste Management, University of Arizona, AZ, 1989,* p. 293.

11. ASME Boiler and Pressure Vessel Code, Section III, Division 1, Case N-510-1, "Borated Stainless Steel for Class CS Core Support Structures and Class 1 Component Supports," December 12, 1994

12. ASME Boiler and Pressure Vessel Code, Section III, Division 3, Case N-728, "Use of B-932-04 plate material for non-pressure retaining spent-fuel containment internals to 650F (343C), Section III, Division 3," May 10, 2005.

13. D.V. Fix, J.C. Estill, L.L. Wong, and R.B. Rebak, "General and Localized Corrosion of Austenitic and Borated Stainless Steels in Simulated Concentrated Ground Waters," *American Society of Mechanical Engineers Pressure Vessels and Piping Division (ASME-PVP) Conference, San Diego, CA, July 2004*.

14. INL DWG 630285, "Crevice Corrosion Specimen," March 15, 2005.

15. Kevin Mon (YMP), (Kevin_Mon@ymp.gov), "Fw: PD," to Ted Lister (INL), (Tedd.Lister@inl.gov), July 24, 2006.

16. PLN-1880, "Experimental Plan for Electrochemical Corrosion Testing of Ni-Cr-Mo-Gd Alloys," Rev. 1, July 13, 2005.

17. PLN-1885, "Experimental Procedures for Corrosion Testing of Ni-Cr-Mo-Gd Alloys," Rev 2, September 1, 2005.

18. ASTM G5-94, "Standard Reference Test Method for Making Potentiostatic and Potentiodynamic Anodic Polarization Measurements," American Society for Testing and Materials, 2004.

19. Sandia National Laboratory, Technical Work Plan for Borated Stainless Steel Testing, DOC.20070206.002, January 2007.

20. C.V. Robino and M.J. Cieslak, "High Temperature Metallurgy of Advanced Borated Stainless Steels," *Metallurgical and Materials Transactions A*, vol. 26, 1995, p. 1673.

21. ASTM G102-89, "Standard Practice for Calculation of Corrosion Rates and Related Information from Electrochemical Measurements," American Society for Testing and Materials, 2004.

22. BSC (Bechtel SAIC Company), "General and Localized Corrosion of the Waste Package Outer Barrier," Las Vegas, Nevada, 2004.

23. ASTM G59-97, "Standard Practice for Conducting Potentiodynamic Polarization Resistance Measurements," American Society for Testing and Materials, 2003.

24. A.J. Bard and L.R. Faulkner, *Electrochemical Methods*, 2nd ed., Wiley, New York, 2001, Chapter 3.

25. D.C. Silverman, *Uhlig's Corrosion Handbook*, 2nd ed., Wiley, New York, 2000, pp. 1197-1198.

26. Electrochemical Corrosion Testing of Neutron Absorber Materials, INL/EXT-06-11772, November 2006.

27. E.A. Loria and H.S. Isaacs, "Type 304 stainless Steel with 0.5% Boron for Storage of Spent Nuclear Fuel", *Journal of Metals*, December 1980, p. 10.

28. A. Kugler, Neutronit A976, Sheet and Plate for Nuclear Engineering, Bohler Bleche GmbH, September 1997.

29. D.V. Fix and R.B. Rebak, "The Long Term Corrosion Test Facility at the Lawrence Livermore National Laboratory," UCRL-Proc-229377, Lawrence Livermore National Laboratory, Livermore, CA. 94550, March 34, 2007.

30. D.A. Moreno, B. Molina, C. Ranninger, F. Montero, and J. Izquierdo, "Microstructural Characterization and Pitting Corrosion Behavior of UNS S30466 Borated Stainless Steel," *Corrosion* 60 (2004) 573.

31. T.E. Lister, R.E. Mizia, P.J. Pinhero, T.L. Trowbridge, and K.B. Delezene-Briggs, "Studies of the Corrosion Properties of Ni-Cr-Mo-Gd Neutron-Absorbing Alloys," *Corrosion,* vol. 61, 2005, p. 706.

Appendix A

A978 PS Test Data

Appendix A

A978 PS Test Data

This supplemental report provides data from tests of A978 specimens. These tests were not included in the main report due to experimental issues with the design of the specimen electrical contact. Two methods were used to make the specimen contact to the non-standard specimens. Specimens for Tests 072706 and 080206 were attached using short platinum wire spot-welded to a corner of the coupon and a longer plastic insulated wire soldered to that wire. Then the entire exposed wire was insulated using Dexter Hydrosol epoxy. Problems were noted during the testing with delamination of the epoxy, leading to corrosion of the wire and solder. With these tests, the initial part of the experiment (E_{corr} measurement, LPR) is likely not affected. However, the PS data is likely affected. It is not known when the delamination affected the test, so the data is of limited use. A second attachment method used a platinum wire (corrosion resistant, but not unreactive) spot welded to a corner of the coupon and extended out of the cell. No coating was used, which left the platinum wire and spot-weld damage exposed to the solution. Tests 082206 and 082806 used this contact, which was stable, but the platinum wire was exposed; thus, it could contribute to the measured current. Table A1 (page 55) shows data tabulated from PS testing of A978 specimens.

Figures A1 and A2 show the E_{corr} measurement for the A978 tests under aerated and N_2 purge. There does not appear to be a consistent common behavior in the E_{corr} data except of the two epoxy coated specimens under N_2 purge.
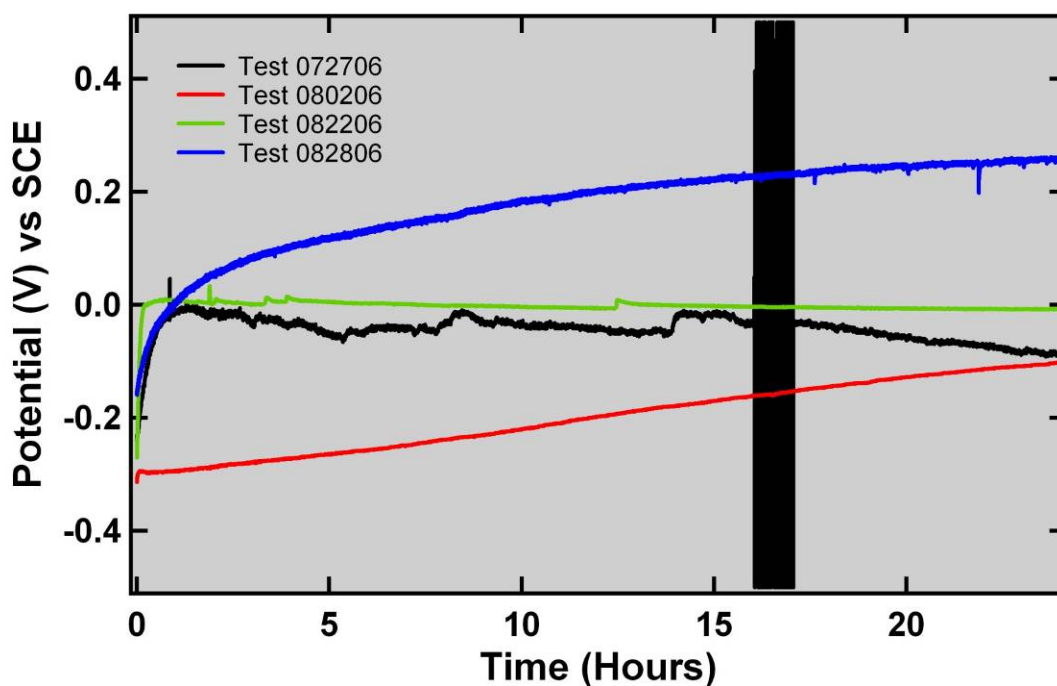

Figure A1. Plots of E_{corr} versus time for A978 specimens with aeration.
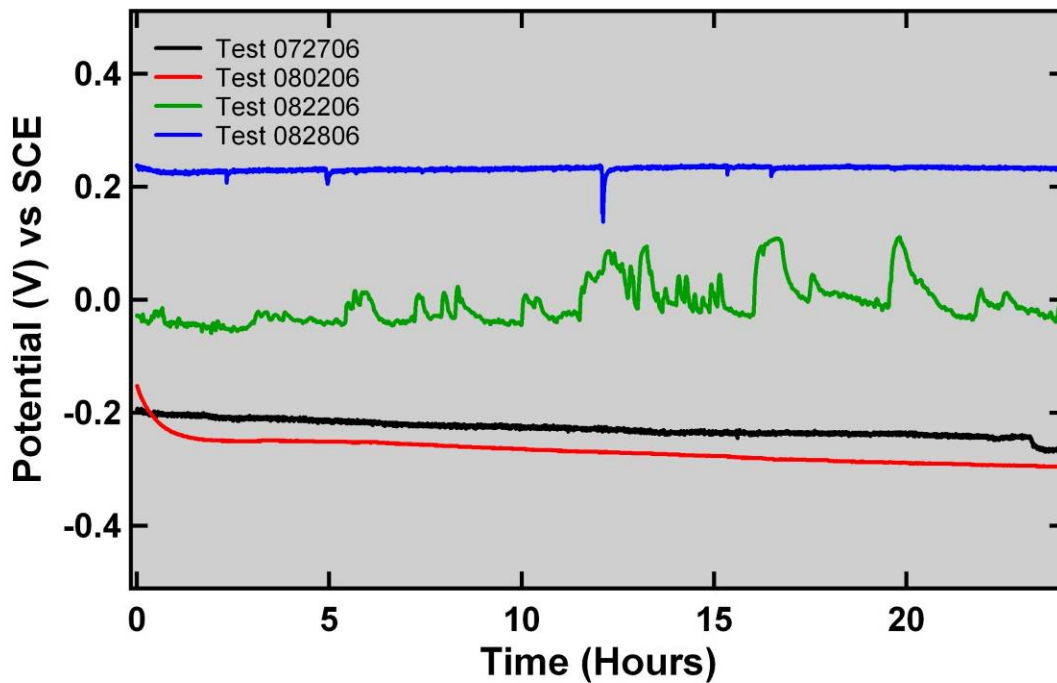
Figure A2. Plots of E_{corr} versus time for A978 specimens during N_2 purge.

Figure A3 shows the PS data obtained from the four A978 specimens. The two specimens using an epoxy coating have much higher current. After examination of the specimens after the test (see Figure A4), it was noticeable that the contact to the specimens was corroded. The specimens using only a bare, platinum-wire contact showed low negative currents with a short positive current excursion due to localized corrosion. This negative current is evidently due to the exposed platinum wire and is likely an electrochemical reaction with dissolved species. Thus, in all cases a corrosion rate cannot be ascertained because the current is dominated by other reactions at the contact wires. Because the net current was negative, this suggests that the anodic corrosion current for the A978 was low.

Figure A4 shows macro photographs of the specimen surfaces after testing. While the electrochemical data was not very useful, the damage to the surface observed during the test is likely to be what would occur on a test using the properly configured crevice specimen. The exception might be Test 072706. The contact was so corroded that the specimen was not in electrical contact for much of the test. A thick brown film coated the surface of the Test 072706 specimen, and the solution was clouded with precipitate. The film appeared to be from the corrosion of the solder and wire of the contacting lead. Significant crevice corrosion was observed only on Tests 080206 and 082206. LOM of damage to these specimens under the crevice formers is shown in Figure A5. There was no significant damage to Test 072706 and 082806 specimens.
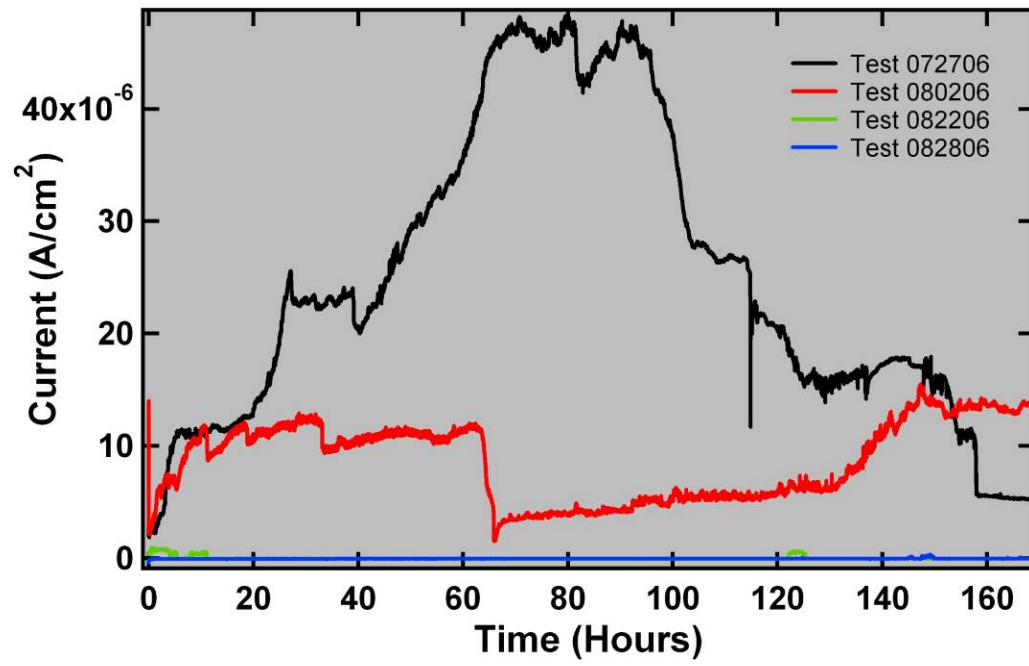
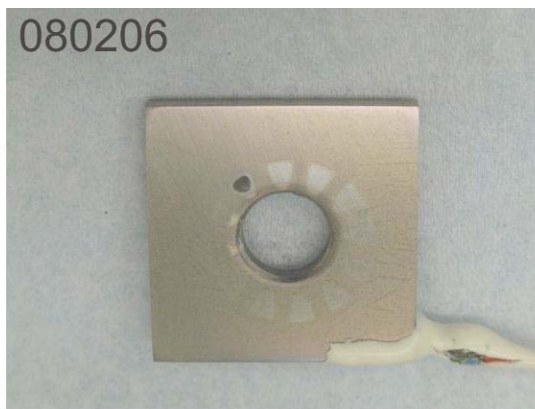Figure A3. Plots of current versus time for PS tests of A978 specimens.

Figure A4. Macro photographs of A978 specimens after testing. Note that part of the platinum wire from the Tests 082206 and 082806 remains in the corner of these specimens.
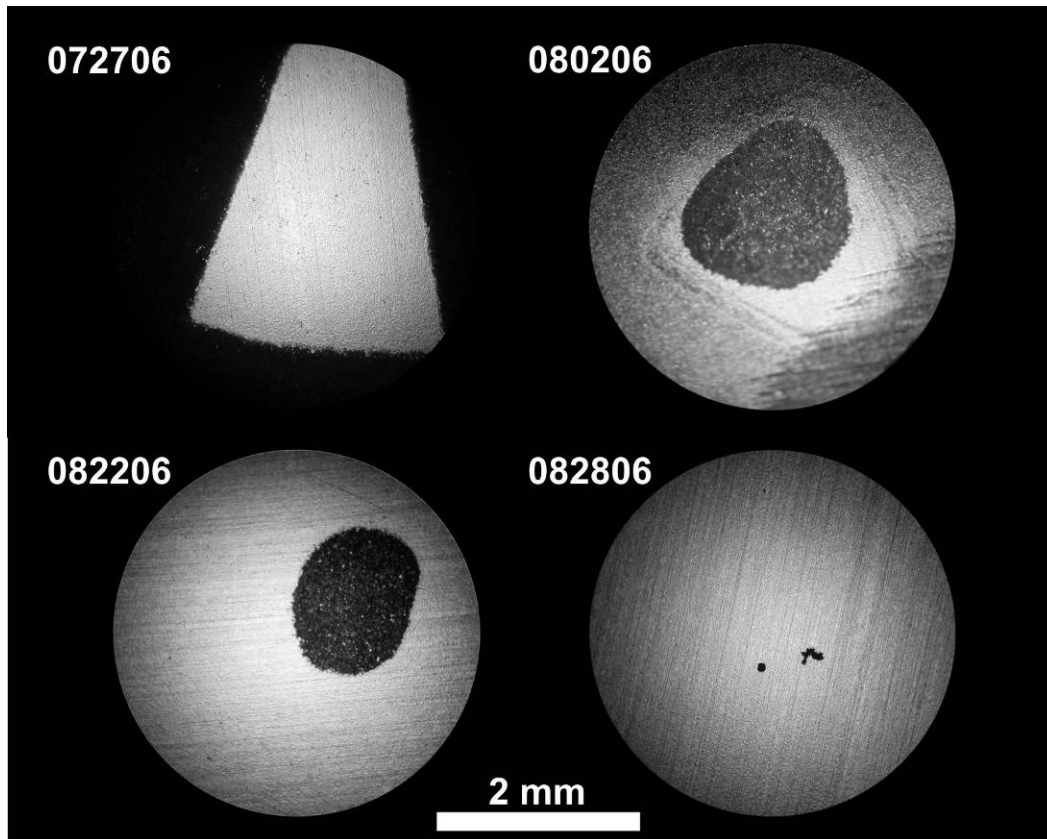
Figure A5. LOM images of A978 specimens after testing.

Table A1. Data for A978 tests.

Test ID	Solution	Final E_{corr} Ox (V)	Final E_{corr} N_2 (V)	LPR CR (μm/yr)	Total Charge (C/cm^2)	Peak Current (A/cm^2)	I_{corr} (A/cm^2)	CR (μm/yr)	EC Test Comments	Solution Observations	Sample Observations
072706	B1	-0.092	-0.265	0.975	14.94	4.82E-05	5.32E-06	52.7	Ox E_{corr} smooth except for one very erratic period, N_2 E_{corr} fairly smooth, bad contact	Orange/Brown with precipitates	Orange film from corrosion of contact, no crevice corrosion
080206	B3	-0.102	-0.2951	1.04	5.22	1.55E-05	2.11E-04	135	E_{corr} smooth, PS very erratic and choppy, bad contact	Clear and colorless	One large crevice pit area
082206	B1	-0.0078	-0.0018	0.657	7.14E-03	9.49E-07	-2.54E-08	N/A	Some pit initiation, negative PS current, interference with platinum	Clear and colorless	Crevice corrosion evident
082806	B3	0.259	0.233	0.196	-0.01409	3.16E-07	-2.22E-08	N/A	Some pit initiation, negative PS current, interference with platinum	Clear and colorless	No crevice corrosion

Note: Tests 072706 and 080206 had corrosion of the specimen contacts leading to excessive currents in the PS tests

Tests 082206 and 082806 had negative i_{corr} values and thus corrosion rate was calculated